Formation of authigenic grey monazite: A palaeo-thermal anomaly marker in very-low grade metamorphic rocks?

Johann Tuduri, Olivier Pourret, Eric Gloaguen, Philippe Lach, Emilie Janots, Sébastien Colin, Jérôme Gouin, Matthieu Chevillard, Laurent Bailly

▶ **To cite this version:**

Johann Tuduri, Olivier Pourret, Eric Gloaguen, Philippe Lach, Emilie Janots, et al.. Formation of authigenic grey monazite: A palaeo-thermal anomaly marker in very-low grade metamorphic rocks?. Ore Geology Reviews, 2023, 160, pp.105583. 10.1016/j.oregeorev.2023.105583 . insu-04181154

HAL Id: insu-04181154
https://insu.hal.science/insu-04181154

Submitted on 15 Aug 2023

HAL is a multi-disciplinary open access archive for the deposit and dissemination of scientific research documents, whether they are published or not. The documents may come from teaching and research institutions in France or abroad, or from public or private research centers.

L'archive ouverte pluridisciplinaire **HAL**, est destinée au dépôt et à la diffusion de documents scientifiques de niveau recherche, publiés ou non, émanant des établissements d'enseignement et de recherche français ou étrangers, des laboratoires publics ou privés.

Distributed under a Creative Commons Attribution - NonCommercial - NoDerivatives 4.0 International License

Ore Geology Reviews 160 (2023) 105583

Contents lists available at ScienceDirect

Ore Geology Reviews

journal homepage: www.elsevier.com/locate/oregeorev

Formation of authigenic grey monazite: A palaeo-thermal anomaly marker in very-low grade metamorphic rocks?

Johann Tuduri [a,b,*], Olivier Pourret [c], Eric Gloaguen [a,b], Philippe Lach [a,b], Emilie Janots [d], Sébastien Colin [a], Jérôme Gouin [e], Matthieu Chevillard [a], Laurent Bailly [a]

[a] BRGM, F-45060 Orléans, France
[b] ISTO, UMR7327, Université d'Orléans, CNRS, BRGM, F-45071 Orléans, France
[c] UniLaSalle, AGHYLE, F-60026 Beauvais, France
[d] Univ. Grenoble Alpes, CNRS, IRD, IFSTTAR, ISTerre, 38000 Grenoble, France
[e] Pôle Avenia, F-64053 Pau, France

ARTICLE INFO

Keywords:
Rare earth elements
Continental shelves
Anchizone metamorphism
Black shales

ABSTRACT

Reassessment of France's rare earth element (REE) potential led us to investigate REE behaviour in the black shales of the Middle Ordovician Angers-Traveusot Formation in central Brittany (France). This study focuses on the distribution of nodular grey monazite (up to 200 g/t) within the shales, which formed in response to the diagenetic and low-grade metamorphic evolution of the studied area. Whole rock geochemistry, rock–eval pyrolysis and evolution of clay mineral crystallinity were firstly used to determine temperature and mass transfer conditions in the black shales. Then, monazite texture, composition and U–Pb in-situ dates were determined, and correlated with the diagenetic/anchimetamorphic conditions. Nodular monazite appears in the Ordovician black shales at the transition between high-grade diagenesis and the anchizone metamorphic facies, in response to processes controlled by competing influences such as organic matter maturation, Fe oxide/hydroxide reduction and clay transformation with accompanying fluid release. Monazite occurs mainly as elongated nodules, up to 2 mm in diameter that are characterised by their grey colour caused by an abundance of host-rock mineral inclusions. Monazite nodule compositions are zoned with Nd and middle REE-rich cores surrounded by Ce-rich rims, with no evidence of inherited domains. Ce-monazite also occurs as a replacement of nodular monazite or in late-stage fractures. Zoned nodular grey monazites were dated at ca. 403.6 ± 2.9 Ma, which is proposed to record the high heat flux that led to the anchimetamorphic conditions found at the base of the Angers-Traveusot formation, prior to the Variscan deformation. Crystallisation of the metamorphic Ce-monazite occurred at two periods, dated at 382.6 ± 2.9 Ma and 349.6 ± 6 Ma, which correspond to pre-collisional and collisional tectono-metamorphic stages respectively. Nodular grey monazite constitutes an interesting alternative economic solution because of its very low content in both Th ($\overline{X}$=2160 ppm) and U ($\overline{X}$=145 ppm) and negligible radiological impact if mined. However, placers currently display a limited economical interest.

1. Introduction

The rare earth elements (REE) are trace elements found in most geological settings, and are particularly useful for understanding a wide variety of geological processes because of their specific properties. For example, the solubility and mineral properties of REE make these elements excellent probes of low temperature geochemical reactions and processes (Johannesson et al., 1997; Michard, 1989; Noack et al., 2014; Pourret and Tuduri, 2017; Rillard et al., 2019; Wood, 1990). Interest in REE geochemistry comes from their chemical properties that often leads to fractionation in geochemical systems (Henderson, 1984). The REE are a group of 15 chemical metallic elements that are coherent in terms of ionic radius, charge (generally occurring in the trivalent oxidation state) and mineral site coordination (Henderson, 1984; Jones et al., 1996; Lipin and McKay, 1989). They include the whole lanthanide group (from La to Lu). Depending on the specific configuration of electrons within each atom, REE are also commonly split into light rare earth elements (LREE: La-Nd), middle rare earth elements (MREE; Sm-Tb) and heavy

* Corresponding author at: BRGM, F-45060 Orléans, France.
E-mail address: j.tuduri@brgm.fr (J. Tuduri).

https://doi.org/10.1016/j.oregeorev.2023.105583
Received 27 July 2022; Received in revised form 19 July 2023; Accepted 21 July 2023
Available online 22 July 2023
0169-1368/© 2023 The Authors. Published by Elsevier B.V. This is an open access article under the CC BY-NC-ND license (http://creativecommons.org/licenses/by-nc-nd/4.0/).

rare earth elements (HREE; Dy-Lu). Because the transition metal yttrium (Y) is chemically similar to elements in the lanthanide group, it is included in the HREE subgroup. Indeed, Y and Ho are referred to as geochemical twins in many geochemical processes.

Monazite [(LREE to MREE, Ca, Th, Y)PO_4] is one of the most significant REE minerals in terms of geochemistry and geochronology (Bea, 1996; Engi, 2017; Montel et al., 1996; Parrish, 1990; Poitrasson et al., 1996). It is a common accessory mineral found in a wide variety of metamorphic and magmatic rock types and is stable from greenschist metamorphic facies up to the highest metamorphic conditions (e.g. Spear and Pyle, 2002). Monazite is resistant to weathering at the Earth's surface, as shown by its widespread occurrence as a detrital mineral in sands and sandstones. Under greenschist and more general low temperature conditions, fluids play a major role in monazite reactivity during both prograde and/or retrograde metamorphic conditions (Janots et al., 2011; Janots et al., 2008; Rasmussen and Muhling, 2007; Read et al., 2002; Seydoux-Guillaume et al., 2012). However, monazite can occur in low-grade metamorphic and diagenetic conditions, where its origin is as yet unresolved. It has variously been interpreted as detrital, diagenetic or anchizonal (Čopjaková et al., 2011; Evans and Zalasiewicz, 1996; Milodowski and Zalasiewicz, 1991; Rosenblum and Mosier, 1983; Wilby et al., 2007). This is especially true for the enigmatic crystallisation of nodular monazite found in shales, which become further concentrated in palaeoplacer and placer deposits in France, Belgium, Portugal, Siberia, Spain, Taiwan, USA, United Kingdom, Iran and a number of African countries (Alipour-Asll et al., 2012; Burnotte et al., 1989; Charles et al., 2022; Cooper et al., 1983; Donnot et al., 1973; García-Tenorio et al., 2018; Milodowski and Zalasiewicz, 1991; Read et al., 1987; Rosenblum and Mosier, 1983; Salgueiro et al., 2020). Published results on the origin of nodular monazite are largely based on the structure and chemistry of nodules recovered from placers (Cobert et al., 2015; Cooper et al., 1983; Donnot et al., 1973; Milodowski and Zalasiewicz, 1991; Read et al., 1987; Rosenblum and Mosier, 1983). Nodular monazite corresponds to millimetric grains that are grey to almost black due to the abundance of micro-inclusions mostly carbonaceous, and commonly exhibit a nodular ellipsoidal morphology. With regard to its chemical composition, nodular monazite is usually enriched in MREE (mostly Eu-Gd) and low in Th and U (Alipour-Asll et al., 2012; Donnot et al., 1973; Rosenblum and Mosier, 1983). These specific characteristics make nodular grey monazite (NGM) of particular interest in mineral exploration and exploitation, because of their low radioactive content, and for the REE + Y which are a critical commodity now widely used in green technologies (Charles et al., 2022; Guyonnet et al., 2016; Lee et al., 2020).

The origin of NGM is still debated, and may be associated with compactional dewatering during sedimentation or low-grade regional metamorphism (Burnotte et al., 1989; Čopjaková et al., 2011; Evans and Zalasiewicz, 1996; Milodowski and Zalasiewicz, 1991). The source of the REE incorporated during NGM crystallisation is also unclear. It may be related to the desorption of REE adsorbed on the surface of clay minerals or Fe oxides/hydroxides, the degradation of organic matter (OM), or the dissolution of detrital REE minerals including monazite, as described for greenschist-facies metasediments (Evans and Zalasiewicz, 1996; Janots et al., 2008; Lev et al., 1998; Milodowski and Zalasiewicz, 1991; Pourret and Tuduri, 2017; Rasmussen and Muhling, 2007). Nevertheless, common features highlight the lack of crustal thickening and prograde metamorphism where NGM occurs and crystallisation temperatures ranging from 200 to 350 °C (*i.e.* very low grade to low grade metamorphic conditions, see references above).

In contrast, studies focusing on the distribution of NGM in sedimentary formations and their links with basin thermicity, fluid generation and tectonic setting are lacking. The aim of this study is therefore to present and discuss the formation of NGM in the light of their distribution within the context of the tectono-metamorphic evolution of the geological domain in which they occur in order to provide mineral exploration strategies. Taking into account mineral and rock geochemistry, quantification of the diagenetic to metamorphic conditions using illite crystallinity, geochronological constraints, together with deformation gradient, a model for the formation of NGM is thus proposed and discussed in light of their implications concerning REE behaviour during diagenesis and low-grade metamorphism.

2. Geological setting

The Armorican Massif (Fig. 1), part of the Ibero-Armorican arc in the late Palaeozoic Variscan belt of Western Europe, comprises three main domains: the Northern, Central and Southern Armorican domains. These domains have different tectonic and metamorphic histories and are bounded by two major dextral shear zones: the North and South Armorican Shear Zones (Ballèvre et al., 2009; Gumiaux et al., 2004; Jégouzo, 1980). Deformation in the Northern Armorican Domain mainly occurred in the Neoproterozoic; this domain was part of the upper brittle crust during the Variscan orogeny (Brun et al., 2001). The Central Armorican Domain, in which NGM are widespread (Fig. 1), is mostly composed of an upper Neoproterozoic to lower Cambrian shale and greywacke basement covered by Palaeozoic siliciclastic sedimentary rocks (Ballèvre et al., 2009). The Southern Armorican domain corresponds to the internal metamorphic zones of the Variscan belt (Ballèvre et al., 2009). The Variscan orogeny developed in the same way in the Central and Southern domains (Ballèvre et al., 2009; Ballèvre et al., 2012; Ballèvre et al., 2013; Paquette et al., 2017). Firstly an oceanic subduction stage took place during the Middle Devonian (*ca.* 380 Ma). This evolved during the late Devonian-early Carboniferous (early Mississippian) into a continental subduction stage (*ca.* 355 Ma) then into a crustal thickening stage (*ca.* 350–340 Ma), during the early and middle Mississippian, followed by an extensional period with numerous leucogranite injections at the Mississippian – Pennsylvanian (late Carboniferous) boundary (*ca.* 330–310 Ma). Both the extension and pluton emplacement were coeval with strike-slip along the South Armorican Shear Zone (Gapais et al., 2015). In the Central Armorican Domain, Palaeozoic rocks, mostly Ordovician in age, were emplaced in response to the opening of the Rheic Ocean between Avalonia and Gondwana from about the late Cambrian (Ballèvre et al., 2009; Nance et al., 2012).

In the study area (Figs. 1–3), the "Initial Red Beds" (Pont-Réan Formation) give way to the Grès Armoricain Formation dated as Floian (early Ordovician), and overlie the Neoproterozoic basement unconformably (Robardet et al., 1994). The formations are made up of quartzarenites, although the upper part of the formation contains larger silty-clay intercalations (Fig. 3). They record a major marine transgression with significant thickness variations (up to 700 m) reflecting the tectonic effects from continental rifting. They were emplaced in an alluvial to deltaic environment evolving in a shelf depositional setting with protection from storm and tidal effects by barriers (Durand and Noblet, 1986; Guillocheau and Rolet, 1982; Suire et al., 1991). From the Middle Ordovician (Dapingian and Darriwilian) and up to the Sandbian (base of the Upper Ordovician), the overlying Angers-Traveusot shales (400–500 m) were deposited, consisting predominantly of silt- and mudstone, including black shales with some intercalations of sandstones, and/or the occurrence of phosphate nodules in the outer shelf sequences (Dabard and Loi, 2012). The Middle Ordovician Angers-Traveusot Formation was deposited in an open-marine storm-dominated shelf environment controlled by more uniform subsidence patterns suggestive of a post-rift setting (Dabard et al., 2007). The geographic distribution of these Middle (Dapingian, Darriwilian) to Upper Ordovician (Sandbian) shelf deposits and associated faunas indicates an increasing depth of water southwards, from near-shore environments to more distal and deeper environments which correspond to the study area (Henry, 1989; Robardet et al., 1994). Following a major fall in sea-level, sedimentation continued during the late Ordovician with the Katian terrigenous facies and the Hirnantian glaciomarine facies (Dabard et al., 2015; Robardet and Doré, 1988). Although a stratigraphic gap has been identified during the early Silurian

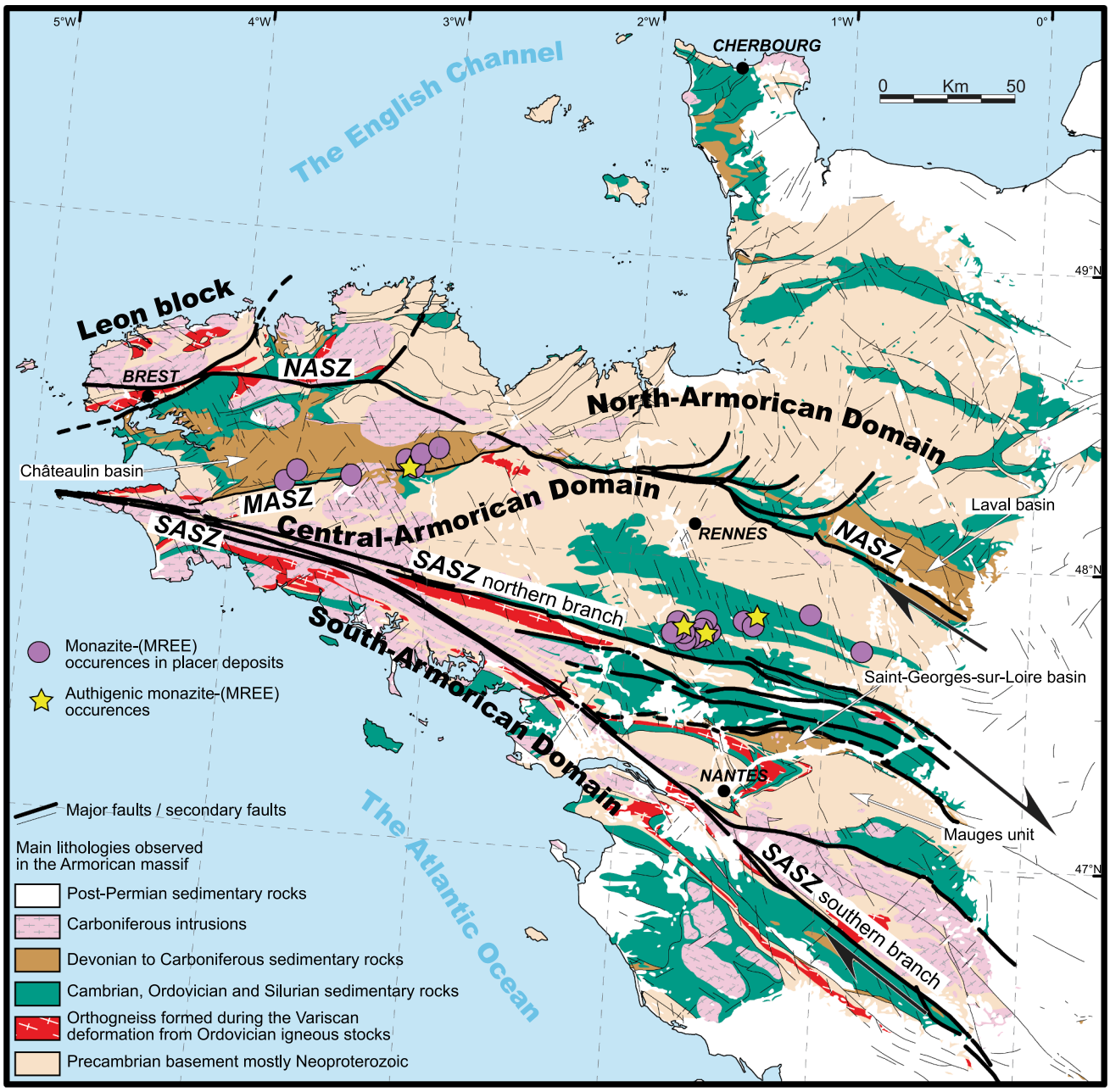

Fig. 1. Simplified map of the main structural domains of the Armorican Massif showing the distribution of authigenic monazite-(MREE) occurrences and those in placers (Geology modified from Chantraine et al., 2003; monazite occurrences from Guigues and Devismes, 1969). NASZ: North Armorican Shear Zone; SASZ: South Armorican Shear Zone.

(Llandovery), marine sedimentary conditions prevailed up to the base of the Lower Devonian (Lochkovian) giving rise to organic-rich shales. From the Pragian to Emsian (Lower Devonian), sedimentary deposits are made up of siliciclastic facies with some intercalated carbonate reefs. Movement along the crustal shear zones bordering the Central Armorican Domain (*i.e.* the North and South Armorican Shear Zones), created Middle Devonian to upper Carboniferous terrigenous and marine depocentres within separate pull-apart basins (e.g. Laval and Chateaulin basins).

Squeezed between these two major structures, the Central Armorican Domain underwent regionally pervasive N120–125-striking dextral deformation that produced upright folds with E–W sub-horizontal axes and sub-vertical axial planes during the Variscan orogeny (Gapais and Le Corre, 1980; Gumiaux et al., 2004). From macro- to microscopic scale, the Central Armorican Domain is affected by marked vertical fracturing (strike-slip faults and extensional fractures) with a dominant N160°E orientation oblique to fold axes (Fig. 4a). Choukroune et al. (1983) demonstrated that this fracturing was compatible and coeval with Carboniferous dextral strike-slip that occurred throughout the Central Armorican Domain via successive incremental deformation during clockwise rotation of the principal strain axes. Strain intensity within the Central Armorican Domain is weak and increases to the north and south, *i.e.* towards the North and South Armorican Shear Zones. In the study area, this regional strain gradient is assumed to be associated with an increase in metamorphism towards the south, *i.e.* both the northern and the southern branch of the South Armorican Shear Zone, with local concentrations due to Variscan granite emplacement (Le Corre, 1975; Le Corre and Le Theoff, 1976). As a consequence, Tartèse et al. (2015) demonstrated using in-situ U-Pb geochronology on both xenotime and monazite that successive hydrothermal events over about 90 Ma, from

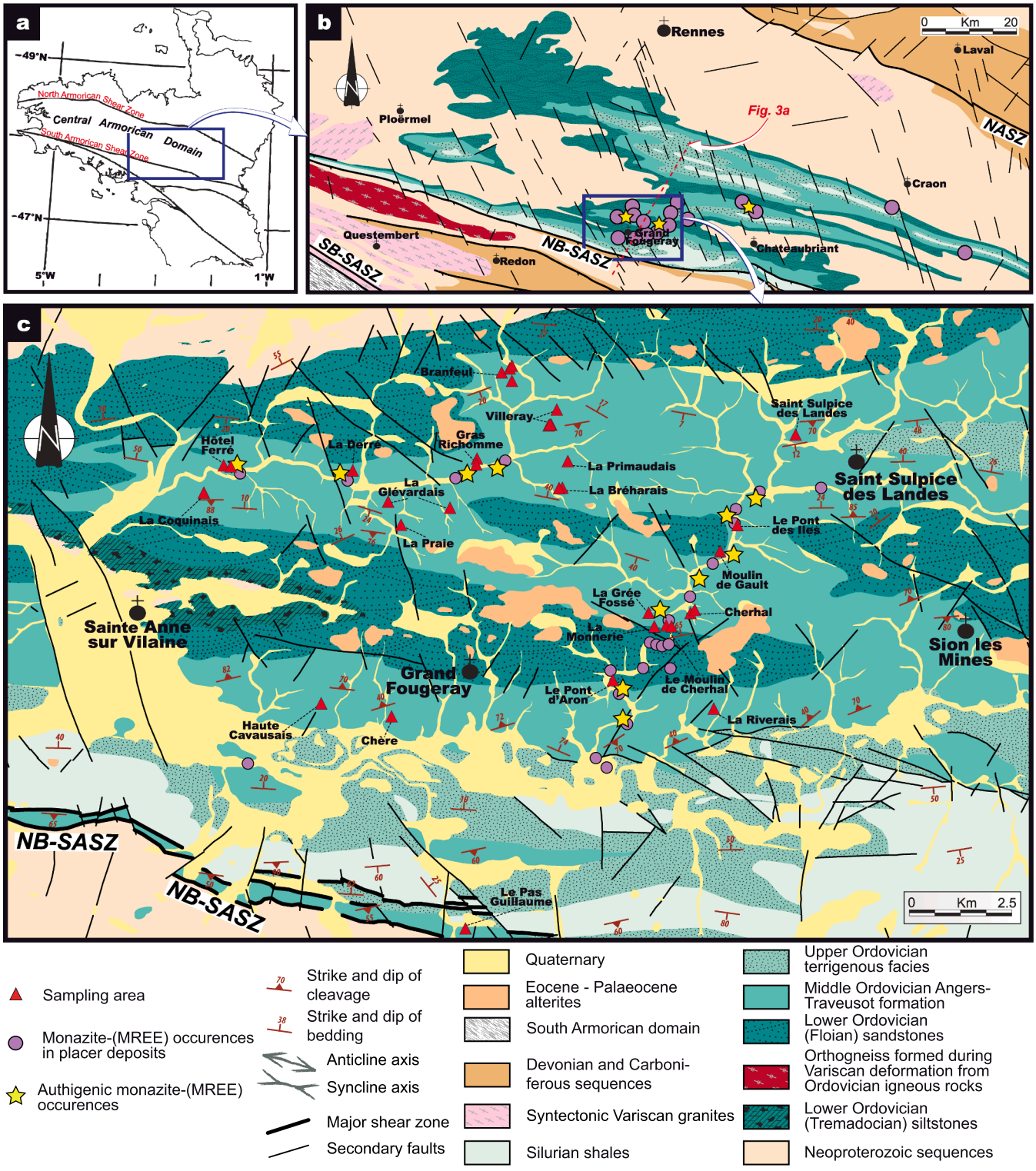

Fig. 2. a) Sketch of the Armorican Massif. b) Regional geological map of the eastern central Armorican domain showing the main geological entities and the study area (modified from Chantraine et al., 2003). C) Geological map of the study area modified from Dadet et al. (1987 and 1995) and Trautmann et al. (1984 and 1987). The Palaeozoic sedimentary formations are folded by long-wavelenght, N110°E-trending upright folds. The succession of synclines and anticlines is controlled by the thick, competent Lower Ordovician Grés Armoricain Formation. Most of the monazite-rich layers were sampled from the Angers-Traveusot Formation (Middle Ordovician black shales). The map uses a Lambert Conformal Conic Projection for France (RGF 1993 Zone 7). NASZ: North Armorican Shear Zone; NB-SASZ: North Branch of the South Armorican Shear Zone; SB-SASZ: South Branch of the South Armorican Shear Zone.

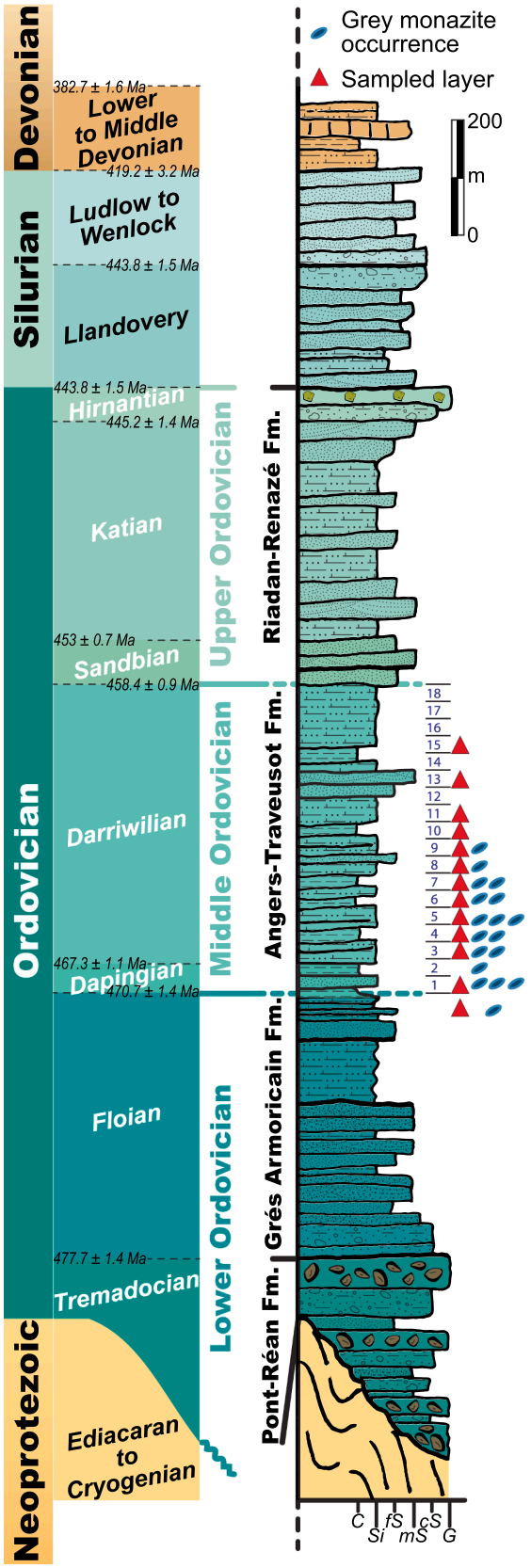

Fig. 3. Lithologic column of the lower Palaeozoic formations observed in the study area (from Dadet et al., 1987; 1995; Trautmann et al., 1984; 1987). Locations of monazite-rich levels and distribution of stratigraphic sequences modelled into 18 levels using the potential-field interpolation method (see below). C: claystone, Si: siltstone, fS: fine sandstone, mS: medium sandstone, cS: coarse sandstone, G: granule; Fm. Formation.

ca. 420 to 330 Ma occurred in the Central Armorican Domain: a time interval that encompasses most of the pre-orogenic and Variscan orogenic phases present in Brittany.

Although several NGM placer deposits have been discovered across the Armorican Massif related to pre-Pennsylvanian sequences (Guigues and Devismes, 1969), only the eastern Central Armorican Domain to the south of Rennes has both numerous placers and authigenic deposits at the same location (Figs. 1 and 2). These NGM occurrences were found during exploratory work by the French Geological Survey (BRGM) in the Middle Ordovician Angers-Traveusot Formation close to Grand-Fougeray (Donnot et al., 1973; Guigues and Devismes, 1969; Guigues and Sapinart, 1967). They are related to low-grade metamorphosed black shales (also named the Angers-Traveusot Formation or Post-olonnec Formation) which are characterized by small grains of quartz, sericite, illite, kaolinite, chlorite and chloritoid that occur together with graphite, pyrite and iron oxides (Donnot et al., 1973), and rarer ilmenite and rutile. Monazite is represented by microcrystalline grey nodules (0.1 to 2.0 mm in size) disseminated throughout the shales. Monazite nodules have been subsequently concentrated in proximal alluvial placers by weathering processes. Within the Ordovician sequence (Figs. 2 and 3), the NGM bearing shales (Angers-Traveusot Formation) overlie oolitic iron formations and sandstones (the Lower Ordovician Grès Armoricain) that are enriched in detrital rutile, ilmenite, zircon and rare monazite (Donnot et al., 1973; Gloaguen et al., 2007; Moëlo et al., 2008). The silty-clay beds of the upper part of the Grès Armoricain Formation at Le Pont d'Aron also host NGM. Donnot et al. (1973) proposed that early diagenesis was of prime importance in the formation of the grey monazite, suggesting the following evolution: (i) precipitation of amorphous REE phosphate in marine silts; (ii) crystallisation into fibrous nodules of rhabdophane; (iii) replacement of rhabdophane by grey monazite-(MREE).

3. Materials and methods

3.1. Sampling

Although the study area comprises mainly lowland fields with very poor outcrop conditions, small abandoned quarries in the area made it possible to establish a sampling strategy. The objective was to evaluate the distribution of NGM grains throughout the Angers-Traveusot Formation and the effects of metamorphism and the deformation gradient. Samples from this formation were therefore collected from 36 outcrops (Fig. 2). Note that three outcrops from the upper part of the Grès Armoricain Formation were sampled as well (Fig. 3). They come from Le Pont d'Aron and La Monnerie areas (Figs. 2 and 3). Heavy NGM concentrates were also sampled from the La Monnerie placer deposit, corresponding to the site of the former BRGM exploration in the 1960s.

3.2. 3D modelling of the Middle Ordovician Angers-Traveusot Formation folds

The pattern of repeated bedding in the Angers-Traveusot Formation created by the intersection of 3D plunging fold features with the surface topography has been divided into stratigraphic sequences of 30 m in thickness (n = 18) according to the potential-field interpolation method implemented in the 3D GeoModeller software (see Calcagno et al. 2008 for method).

3.3. X-ray diffraction analysis and Kübler index

Major mineral assemblages (quartz, feldspars, oxides and sheet silicates) were characterized optically using thin sections under the optical microscope and by X-ray diffraction (XRD) analysis. XRD analysis was carried out on representative crushed rock samples at the UniLaSalle Institute using a D8-Advance Bruker-AXS diffractometer (Siemens). Twenty-one samples of the Angers-Traveusot Formation (Grand

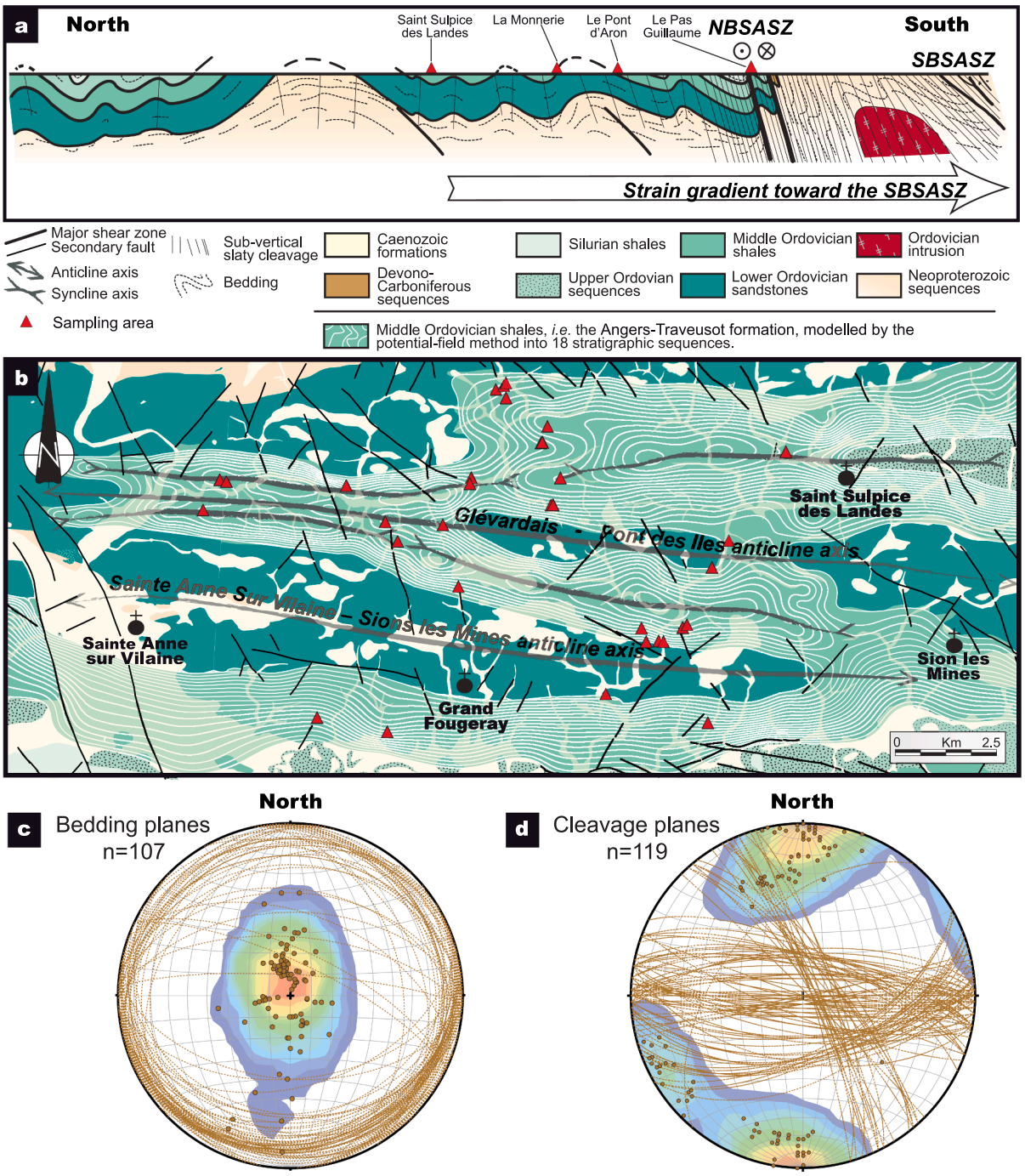

Fig. 4. a) A simplified cross-section of the eastern part of the central armoricain domain. The northern branch of the north-armorican shear zone cuts across a sequence of beds whose deformation increases north-south. b) Simplified geological map of the Grand Fougeray area. Main fold axes are highlighted such as the Sainte Anne sur Vilaine – Sions les Mines anticline axis. The Angers-Traveusot Formation has been subdivided into 18 stratigraphic sequences using the potential-field interpolation method. Stereographic projections (Schmidt's lower hemisphere equal-area projection) of (c) bedding planes of Palaeozoic sedimentary rocks and (d) cleavage planes. Planes are represented by their respective poles and density plots.

Fougeray area) and eight samples from the upper part of the Grès Armoricain silty-clay Formation (Le Pont d'Aron area, Fig. 2b, 3 and 5) were selected for calculation of their Kübler-Index (KI) and Árkai-Index (ÁI) from the full width at half maximum of illite/muscovite and chlorite on the air-dry powder diagram respectively. Full operating conditions and data are reported in Supplementary Appendix 1 and 2 respectively.

3.4. Whole rock analyses

Whole-rock chemical analyses were performed on crushed and pulverized shale samples at the Bureau Veritas Laboratories (Vancouver, Canada, formerly Acme Analytical Laboratories). Major oxides and trace elements were determined using ICP-MS. Loss on ignition (LOI) was calculated by weight difference after ignition at 1000 °C. Total abundances of the major oxides and several minor elements are given for a 0.2 g sample analysed by ICP Emission Spectrometry following lithium metaborate/tetraborate fusion and dilute nitric digestion. Rare earth and refractory elements were determined by ICP Mass Spectrometry (ICP-MS) following lithium metaborate/tetraborate fusion and dilute nitric digestion of a 0.2 g sample. Total carbon was determined using

LECO. Data are reported in Supplementary Appendix 3.

3.5. Analysis of carbonaceous materials

Rock Eval 6 pyrolysis (Vinci Technologies®) was performed at the ISTO laboratory (CNRS / University of Orléans, France) under standard conditions with a linear temperature increase program of 30 °C min^{-1} (Lafargue et al., 1998). The final temperature reached in the pyrolysis oven was 650 °C, and 750 °C in the oxidation oven. This analysis provides the following parameters: Total Organic Carbon (TOC, expressed in wt. %), the temperature at which the maximum rate of hydrocarbon (HC) generation occurs in a kerogen sample during the pyrolysis analysis (Tmax, expressed in °C), the Hydrogen Index (HI, expressed in mg HC/g TOC), the Oxygen Index (OI, expressed in mg CO_2/g TOC) and the S2 peak parameter (expressed in mg HC/g rock). Data are reported in Supplementary Appendix 4.

3.6. Scanning electron microscopy, cathodoluminescence and electron probe microanalysis

Monazite grains were studied in detail at the ISTO-BRGM laboratory in Orléans using a Tescan Mira 3 XMU (Tescan, Brno, Czech Republic) scanning electron microscope (SEM) along with optical reflected and transmitted light imaging. The SEM is coupled to a back-scattered electron (BSE) and a panchromatic cathodoluminescence (CL) detector (350–650 nm, TESCAN BSE/CL detector) to produce images for the assessment of compositional variation and textures. Additional SEM-EDX information about mineral inclusions was determined as well.

Monazite and xenotime compositions were determined using the Cameca SX50 electron probe micro-analyser (EPMA) at the ISTO-BRGM laboratory in Orléans. Over 200 analyses were performed but only 119 are used here. An accelerating voltage of 20 kV, a beam current of 100 nA and a 1–2 μm beam width were employed for measurement. La Lα, Ce Lα, Th Mα, Ca Kα were analysed using a PET (Pentaerythritol) crystal. Pr Lβ, Nd Lα, Sm Lα, Eu Lβ, Gd Lβ, Fe Kα were analysed using a LiF (Lithium fluoride) crystal, whereas P Kα, Si Kα and Y Lα were analysed using a TAP (Thallium acid phthalate) crystal. X-ray elemental maps were also recorded with an accelerating voltage of 20 kV and beam current of 100 nA, using the wavelength dispersive spectrometers. Standards used included both well-characterized natural minerals (Durango apatite for Ca, Amelia albite for Na) and synthetic phases for other elements (Fe_2O_3 for Fe, $LaPO_4$ for La, $CePO_4$ for Ce, $PrPO_4$ for Pr, $NdPO_4$ for both Nd and P, $SmPO_4$ for Sm, $EuPO_4$ for Eu, $GdPO_4$ for Gd, YPO_4 for Y and ThO_2 for Th). Counting times were 40 s for each element. For all the chemical compositions, only the significant values with an accuracy of 95% [(peak-background) × counting time $> 2\times\sqrt{}$ (background × counting time)] were retained. The EPMA analysis of Eu was made very difficult due to the existence of several interferences with other lanthanides. In particular, the Lα and Lβ emission peaks (and the corresponding background measurements) are likely to interfere with several Nd, Sm or Gd L peaks. Thus, Eu analyses were discarded. Although HREE are not analysable using EPMA, this method was chosen since a characteristic of NGM is their huge abundance of micro-inclusions which restricts the use of the large sampling volume of laser ablation inductively coupled plasma mass spectrometry (LA-ICP-MS). Thus, due to its better spatial resolution, we consider EPMA to be a reliable in-situ method for obtaining quantitative data of monazite. However, because HREE, Th, U and Pb concentrations are very low or undetectable, average values for these trace elements as well as their interrelationships were further evaluated using LA-ICP-MS. Full operating conditions and results are reported in Supplementary Appendix 1 and 5 respectively.

3.7. U-Th-Pb geochronology

Two different analytical protocols were used for both heavy NGM grains from the La Monnerie placer deposit, and the monazite specimens observed in polished thin sections. Grains were imaged using SEM BSE-CL and all in-situ LA-ICP-MS analyses were carried out at laboratory facilities in Orléans (France).

i) Heavy monazite grains from concentrate were hand-picked under a binocular microscope, then mounted in epoxy resin and subsequently ground and polished until the crystal centres of the grains were exposed along a flat surface. In-situ LA-ICP-MS analyses werecarried out at the French Geological Survey (BRGM) laboratory in Orléans (France). Polished sections were analysed using an ICP-MS X series II spectrometer (Thermofisher) set up in Xs lens, coupled with a Cetac Excite 193 nm laser system. Samples were placed in a dual-volume laser ablation cell.
ii) For polished thin sections, dating was carried out at the ISTO laboratory (CNRS / University of Orléans, France). Monazite grains were analysed using an ICP-MS 8900 (Agilent) coupled to a laser asi® RESOLution Excite 193 nm. LA-ICP-MS U–Pb geochronology of large monazite grains mounted on the polished section was carried out with a nominal spot diameter of 15 μm whereas smaller monazite grains in thin section were analysed with a nominal spot diameter of 10 μm for higher resolution analysis.

Analyses were standardised with respect to the Trebilcock monazite (272 ± 2 Ma, Tomascak et al., 1996). Reproducibility and accuracy of the corrections were controlled through repeated measurements of the Madmon (523 ± 12 Ma, Schulz et al., 2007) and Namaqualand (1033 Ma, Knoper et al., 2000) monazites. Data reduction was carried out using Glitter® software and no common lead correction was applied. The results were generated using IsoplotR by Vermeesch (2018) at 95% confidence and 2σ errors. Note that electron microprobe monazite geochronology was not carried out given the strong concentration of common Pb in these NGM grains.

The same monazites selected for U–Th–Pb dating were analysed in-situ in polished sections and polished thin sections for REE concentrations. Monazite trace-element concentrations were acquired on a Agilent 8900® quadrupole-ICP-MS, coupled with a laser ablation system (CETAC Excite 193 nm) at the BRGM laboratory. The detailed analytical parameters for the ICP-MS and the laser ablation system are listed in Supplementary Appendix 1. Laser spots for REE-analysis were sited next to the pits formed during the U–Th–Pb analyses. Data reduction was carried out with the Glitter software. The Madmon Monazite standard (Schulz et al., 2007) was used as external calibration standard for instrumental drift correction, and phosphorus contents obtained by EPMA were used as internal standard for quantification. Running conditions and data tables are documented in Supplementary Appendix 1 and 6 respectively, whereas Appendix 7 shows the location of the LA-ICP-MS U-Pb analyses.

4. Results

4.1. Field constraints

In the eastern Central Armorican Domain, south of Rennes (Fig. 2), Palaeozoic sedimentary rocks are mainly exposed in small relatively well preserved quarries. The Angers-Traveusot Formation is mainly composed of black shales (Fig. 3), oxidised in places, and contains numerous siliceous nodules and fossils of graptolites, conodonts and trilobites. As described in the literature (Ballèvre et al., 2009; Gapais and Le Corre, 1980; Gumiaux et al., 2004; Jégouzo, 1980; Le Corre et al., 1991; Le Corre and Le Theoff, 1976), the strata have an uniform ESE strike with a broad low dip toward both the north (22°) and south (17°) suggesting an upright fold system with a ca. N110°E-trending fold axis (Fig. 4a, b, c). The strikes and/or dip directions are disturbed locally by an asymmetric plunging fold geometry (the north-directed limb is moderately inclined: ca. 30–50°), periclinal endings, or tilting along NW-SE vertical faults (Fig. 2b, 4b). Folds are associated with an axial-

plane slaty cleavage that is roughly vertical with an E-W to N110°E strike (Fig. 4d). The strike of the cleavage is deflected locally along NW-SE-trending faults (Fig. 4d). A discrete sub-horizontal stretching lineation is observed, which is more clearly visible south of the town of Grand Fougeray, in the vicinity of the northern branch of the South Armorican Shear Zone, suggesting that deformation increases southward and reaches a maximum along the South Armorican Shear Zones (Fig. 1).

4.2. Mineral characterisation, Kübler and Árkai-Indexes

The Angers-Traveusot shale beds appear to be generally uniform, although occasional silty lenses or beds are intercalated over a thickness of a few meters. The rocks are made up of varying modal proportions of quartz (from 26 to 65 %, with mean - $\overline{X}$ - and standard deviation of 46 % $\pm$ 11), with some feldspar mostly plagioclase (3 to 39 %, $\overline{X} = 11.4\ \% \pm 11$), in a clay mineral matrix (13 to 69 %, $\overline{X}$ 42.5 % $\pm$ 12) consisting of a very fine-grained mixture of kaolinite, interstratified illite/smectite, chlorite (chamosite-clinochlore and rare corrensite) and sericite. According to the potential-field interpolation method, the illite/smectite ratio is higher in the lower part of the Angers-Traveusot Formation. Note there is no clear correlation between the distribution and modal proportion of chlorite and the strain gradient, and that sericite may be detrital flakes of 2 M_1 muscovite or an authigenic illite/muscovite

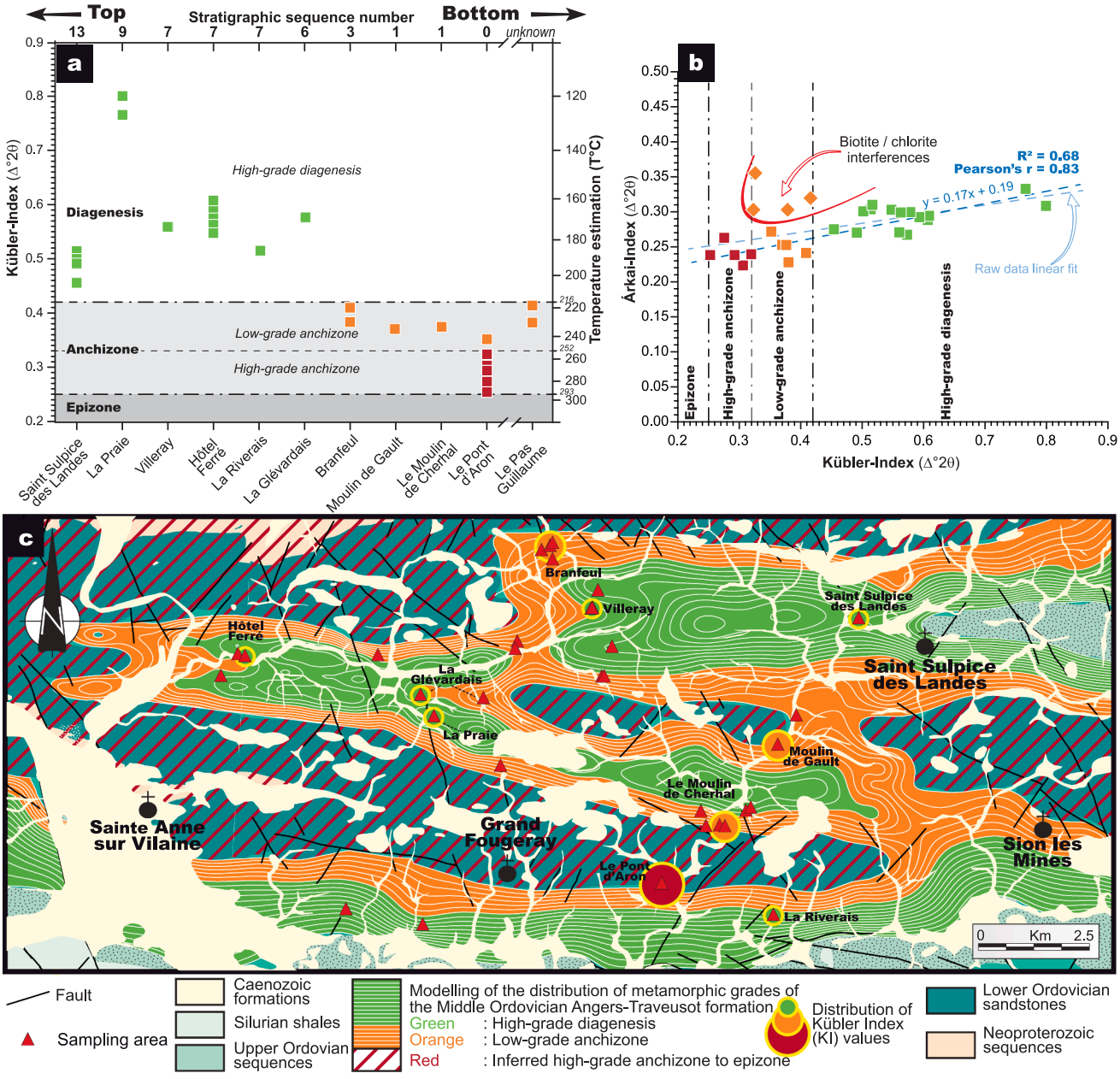

Fig. 5. a) Distribution pattern of Kübler Index (KI) for samples from the Angers-Traveusot and the upper part of the Grés Armoricain Formations in the Grand Fougeray area as a function of their position in the modelled stratigraphic sequences. (b) Correlation between KI (10 Å) and ÁI (7 Å) values. Data with probable biotite interference have been excluded from the calculated correlation coefficient. c) Distribution of metamorphic grades based on KI values overlaid onto a simplified geological map of the Grand Fougeray area. The diagenetic and lower anchizone domains are modelled within the Angers-Traveusot Formation according to the potential-field interpolation method. Location of the upper anchizone and epizone domains in the Lower Ordovician sequences and older units is inferred from data observed in Le Pont d'Aron area and from Le Corre (1975). Metamorphic zone boundaries for KI values are from Warr and Ferreiro Mählmann (2015). Palaeotemperature estimation for KI are from Zhu et al. (2016).

assemblage. Biotite is scarce, although most frequent in the upper part of the Grès Armoricain silty-clay Formation of Le Pont d'Aron. Opaque minerals (pyrite, iron oxides), apatite, rutile, titanite and zircon, with grey monazite are common accessories. Note that pyrite is frequently oxidised and replaced by iron oxides.

The KI values determined for the Angers-Traveusot and the upper part of the Grès Armoricain formations range from 0.80 to 0.25 Δ°2θ, corresponding to metamorphic grades evolving downwards through the stratigraphic sequences from diagenetic to the anchizone and epizone transition respectively (Fig. 5a; Supplementary Appendix 2). The correlation between the KI and ÁI shows some outliers (Fig. 5b), mostly in the anchizone domain, which are attributed to possible interferences from chloritised biotite, and/or differences in successive chlorite crystallisation with different compositions (*i.e.* clinoclore vs. chamosite). When the outlier data is excluded, correlation is good (R^2 = 0.68, Pearson's r = 0.83), with both indexes showing concomitant evolution with increasing metamorphism (Fig. 5b).

In terms of the distribution of metamorphic grades (Fig. 5a), KI values tend to decrease from the upper part of the Angers-Traveusot Formation to the Grès Armoricain boundary where high-grade anchizonal and probable epizonal metamorphic conditions are reached in Le Pont d'Aron area. Indeed, very low-grade metamorphic conditions with the highest KI values (diagenesis) are mostly located in the upper two-thirds of the Angers-Traveusot Formation, whereas lower anchizone conditions are more prevalent in the lower third of this formation. It should be noted that KI values from Saint Sulpice des Landes are low with respect to its position in the upper part of the stratigraphic sequence. This might be the result of local geological features (e.g. unidentified faults concentrating fluid circulation that altered the rocks) or analytical bias. Analytical bias may also explain the unusually high KI value for La Praie. This result is consistent with Le Corre (1975), and helps us infer the distribution of the upper anchizone and epizone domains in the Lower Ordovician sequences and older units (Fig. 5c). The potential-field interpolation method integrating the KI values highlights the upright folds with E–W sub-horizontal axes and suggests an increase in metamorphic grade downwards through the stratigraphic sequence (Fig. 5c). There is no relationship between the metamorphic conditions and the position in the sequence to the northern branch of the South Armorican Shear Zone.

4.3. Geochemical features of the Middle Ordovician Angers-Traveusot Formation

Whole rock geochemistry of black shale samples (Supplementary Appendix 3) from 35 localities (Fig. 2b) shows a relatively uniform chemical composition in terms of both major and trace elements. Using the KI distribution pattern from the potential-field interpolation method, we have adopted the following colour-code in subsequent

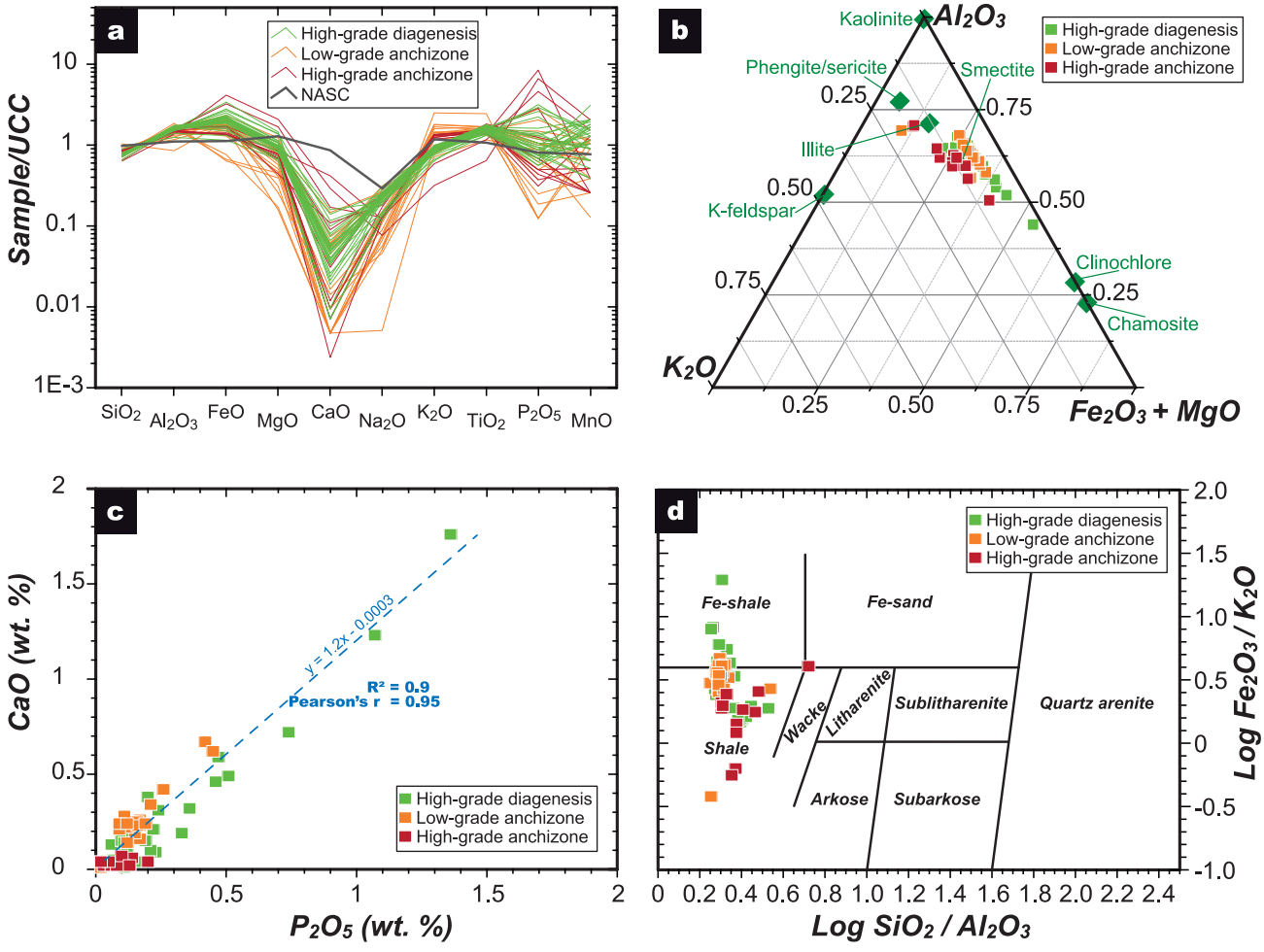

Fig. 6. a) Major element enrichment of shales formations from the grand fougeray area normalized to upper continental crust (UCC). b) Al2O3/K2O/(Fe2O3+MgO) ternary ternary diagram for all analysed shales. c) CaO versus P_2O_5 element distribution. Samples from the high-grade anchizone do not correlate well with the other domains, so they are not used in the correlation coefficient calculation. d) Log SiO2/Al2O3 versus log Fe2O3/K2O geochemical classification plot for sedimentary rocks from Herron (1988). Data are coded green, orange or red based on their provenance from the Lower and Middle Ordovician formations (high-grade diagenesis, low- and high-grade anchizone domains respectively as in Fig. 5b).

figures: in red, samples belonging to the high-grade anchizone/epizone domain (*i.e.* the upper part of the Grès Armoricain Formation); in orange, samples from the low-grade anchizone domain of the Angers-Traveusot Formation; and in green, samples from the high-grade diagenetic domain of the same formation.

4.3.1. Major element geochemistry

The bulk chemical composition of the formation is slightly heterogeneous, although consistent with known shale compositions (Fig. 6a). SiO_2 (from 42.1 to 68.3 wt%, $\overline{X} = 51.6 \pm 4.6$ wt%) and Al_2O_3 (from 13 to 28.3 wt%, $\overline{X} = 24.1 \pm 2.4$ wt%) are the dominant constituents in the majority of the samples. Because these oxides are negatively correlated,

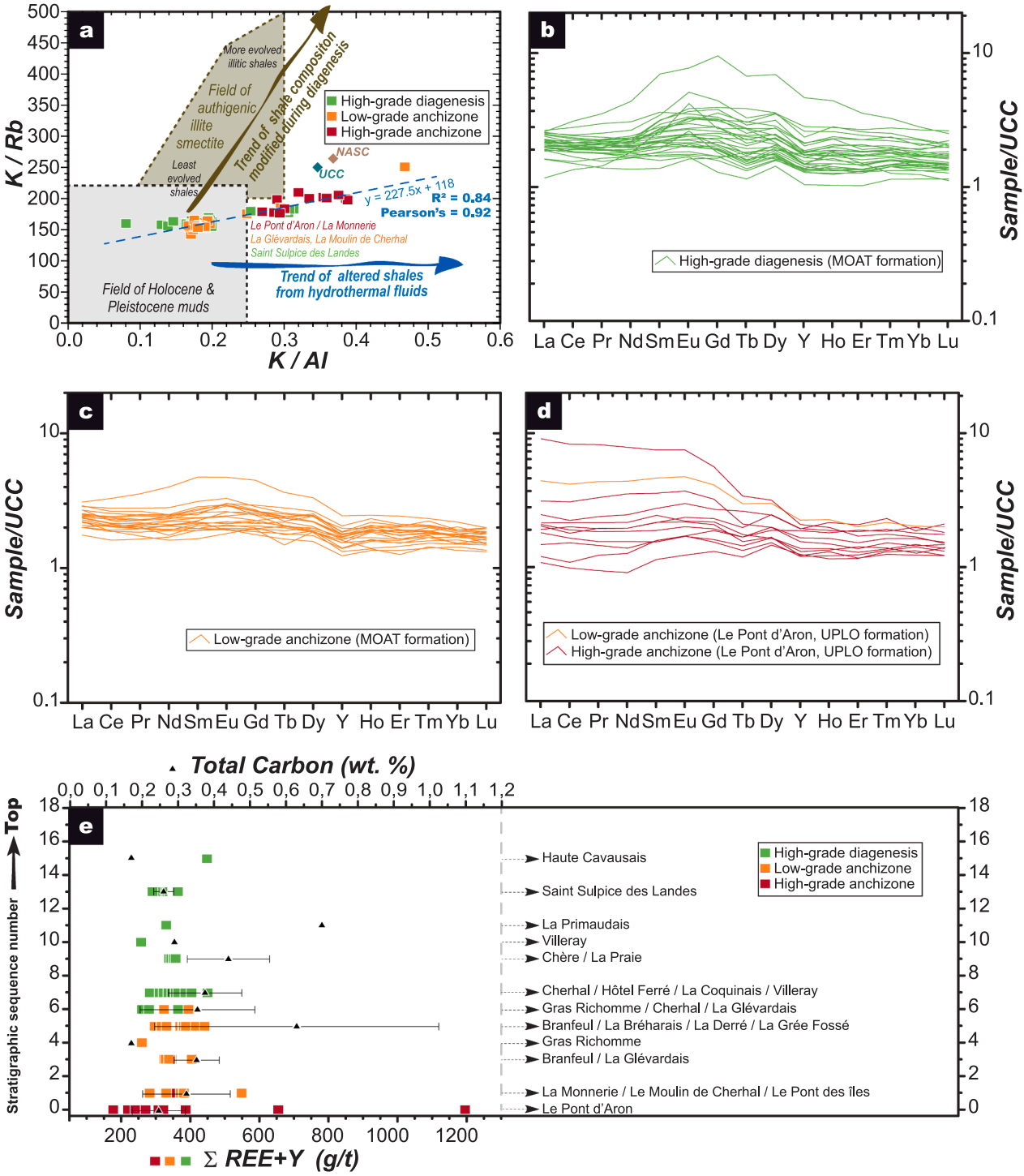

Fig. 7. a) K/Rb versus K/Al for muds and shales from van de Kamp, (2016). Most detrital clays plot within the range of $0.0 < K/Al < 0.25$ and $0 < K/Rb < 220$. Diagenetically modified shales with additional K and Rb commonly form a distinct field outside this range. UCC-normalised REE patterns in samples from b) the diagenetic domain c) the lower anchizone domain, and d) the upper anchizone domain. UCC values are from McLennan (2001). e) Distribution pattern of ΣREE + Y concentrations (square) and total carbon (triangle) in rocks from the Grand Fougeray area as a function of their position in the modelled stratigraphic sequence (using the same key as in Fig. 5b). Total carbon is shown as the mean (black triangle) with the standard deviation (solid black line). Data are presented with respect to their provenance in the Middle Ordovician Angers-Traveusot (MOAT) and the upper part of the Lower Ordovician – Grés Armoricain (UPLO) formations.

the considerable increase in SiO_2 content shown by the Angers-Traveusot Formation highlights the lithological heterogeneity, and represents a quartz-enriched end member. The FeO_T content is heterogeneous and varies from 2.9 to 18.8 wt% ($\overline{X}$=8.6 ± 0.26 wt%). The FeO_T appears to be slightly enriched with respect to the Upper Continental Crust composition (UCC; McLennan, 2001), but while samples from the diagenetic domain (*i.e.* the upper part of the Angers-Traveusot Formation) are homogeneous, the ones from the anchizone domain are more heterogeneous (Fig. 6a). In contrast, the CaO content (from 0 to 1.8 wt%, $\overline{X}$ = 0.23 ± 0.3 wt%) is very low with a moderate to strong depletion compared to UCC. The samples from the anchizone domain (*i.e.* the lower part of the Angers-Traveusot Formation) are, on average, the most depleted in CaO, MgO and also Na_2O, but they are enriched in K_2O (Fig. 6a). Conversely, the P_2O_5 content is variable and displays both positive and negative anomalies: the diagenetic samples are similar to UCC compositon in terms of P content, while samples from the lower anchizone domain are depleted, and samples from the high-grade anchizone are enriched (Fig. 6a).

Variations in Al_2O_3, K_2O and Na_2O may indicate either the presence of feldspar in high-SiO_2 samples (silty layers), or phyllosilicates (illite, chlorite and detrital muscovite). On a Al_2O_3, K_2O and Fe_2O_3 + MgO ternary diagram (Fig. 6b), the data plot between the chlorite – phengite/sericite endmembers, suggesting that the rock-forming minerals are controlled by aluminous phases, in particular illite–smectite and chlorite. In the Angers-Traveusot Formation, P_2O_5 and CaO are very highly correlated ($R^2 = 0.9$, Pearson's r = 0.95, Fig. 6c), with a CaO/P_2O_5 ratio of about 1.2. This may indicate the presence of apatite ($Ca_5(PO_4)_3(OH, F, Cl)$ which has a CaO/P_2O_5 of about 1.3. Note that this is not true of the upper anchizone domain, *i.e.* rocks belonging to the underlying upper part of the Grès Armoricain silty-clay Formation, where CaO is very low. This precludes the occurrence of any carbonate such as calcite in the two units. Based on the geochemical classification of terrigenous sandstones and shales (Herron, 1988), and given most samples have $0.2 < \text{Log}(SiO_2/Al_2O_3) < 0.6$ and $-0.4 < \text{Log}(Fe_2O_3/Al_2O_3) < 1.3$, the samples in this study consist of shales and Fe-shales (Fig. 6d). Iron-shales are mostly observed in the upper part of the Angers-Traveusot Formation (*i.e.* the diagenetic domain, Fig. 5). Wackes are scarce (1 sample), found only in La Monnerie area, *i.e.* the upper part of the Grès Armoricain Formation.

4.3.2. Trace element geochemistry

The plot of K/Rb versus K/Al (Fig. 7a) shows a field for modern sediments (muds). During burial, such sediments are transformed into shales, which then undergo progressive mineralogical changes including phyllic paragenesis in which Al-rich phases such as kaolinite and smectite evolve into K-enriched phases such as illite, muscovite/biotite and K-feldspar. The sediments may also undergo hydrothermal alteration in open system conditions. By analysing the K/Rb ratio, it is possible to use both K and Rb as proxies for metasomatic processes during diagenesis (van de Kamp, 2016). The K/Rb versus K/Al plot for the Angers-Traveusot and the underlying upper part of the Grès Armoricain silty-clay formations, shows a trend with strong positive correlations ($R^2 = 0.84$ and Pearson's r = 0.92) suggesting a slight K enrichment particularly for samples from the high-grade anchizone (Fig. 7a).

The REE + Y distribution highlights key features concerning the origin of the samples with respect to their position in the sequence and the metamorphic grade distribution. For instance, differentiation can be observed in the REE + Y patterns for samples from the diagenetic (Fig. 7b) and low-grade anchizone metamorphic grades (Fig. 7c), which show MREE enrichment. More precisely, there is either a Eu and a Dy positive anomaly (Fig. 7b-c). These patterns exhibiting a slight to moderate downward concavity with an apex at Gd may be enriched by up to one order of magnitude relative to the UCC values. In contrast, the REE + Y patterns for the upper anchizone domain are slightly to highly enriched in LREE sometimes accompanied by a slight negative Ce anomaly (Fig. 7d) and occasional slight enrichment in MREE. Except for some REE + Y enrichment in the upper part of the Grès Armoricain, the ∑REE + Y distribution in rocks is generally homogeneous in the Angers-Traveusot Formation (Fig. 7e). The ∑REE + Y concentrations vary from 177 to 1195 g/t ($\overline{X}$=365 ± 133 g/t).

4.3.3. Total carbon and total organic carbon

Whole rock total carbon and total organic carbon concentrations are given in Supplementary Appendixes 3 and 4. Total carbon (TC) content ranges from 0.13 to 1.2 wt% ($\overline{X}$=037 ± 0.2 wt% TC), while TOC content ranges from 0.1 to 1.1 wt% ($\overline{X}$=0.4 ± 0.2 wt% TOC). TOC and TC show a high positive correlation ($R^2 = 0.93$, Pearson's r = 0.97, Fig. 8a), with a slope of about 0.93. This confirms that the amount of inorganic carbon, e.g. in a carbonate phase, is very low, calculated at between 0 and 0.15 wt%. Therefore, almost all the C in the Angers-Traveusot Formation is organic in origin.

In the ∑REE + Y versus TC graph, most samples plot along a positive slope suggesting a possible evolution of REE + Y with increasing organic carbon (Fig. 8b). The marked scattering along the y axis may be interpreted as pore fluid migration according to Rasmussen et al. (1998). Although pore fluid migration does not seem to be a common process (Fig. 8b), the Pont d'Aron and Saint Sulpice des Landes samples which have been affected by K-metasomatism, are also preferentially affected by pore fluid migration processes (Fig. 7a). With a mean of 0.37 wt% for the TOC content, the HC potential is inferred to be poor despite some moderately rich source samples, as shown by combining TOC and S_2 values (Fig. 8c). When a source rock matures, the amount of OM in the source rock decreases in terms of both the TOC content and the amount of reactive kerogen (Rock-Eval S2). The Tmax distribution in the S_2 versus TOC diagram, should define a general trend of maturity with the highest temperatures corresponding to both low TOC and S_2 values. However, the absence of any clear correlation (Fig. 8c) suggests that the majority of samples have undergone alteration. In the pseudo-Van Krevelen diagram (Fig. 8d), the samples form a cluster within the type IV kerogen field. This reinforces the hypothesis that most samples have been altered, probably by weathering and oxidation. Nevertheless, the samples with a type III kerogen signature will be discussed below, in section 5.2 (Fig. 8d).

4.4. Monazite occurrences and geochemistry

Although it is only an accessory mineral, monazite is visible to the naked eye in the field in both the Angers-Traveusot and the upper part of the Grès Armoricain formations (Fig. 9a, b). Because monazite is very dense ($d \gg 4.5$ g/cm^3), occurs as fairly large nodules (up to 1.5 mm) and is resistant to weathering processes, these heavy mineral grains can be concentrated in placer deposits (Fig. 9c). Exploration a few decades ago, using Banka drilling equipment, revealed heterogeneous concentrations in some placer deposits (Donnot et al., 1973; Guigues and Sapinart, 1967). The richest sites are all located along the Glévardais – Pont des Iles anticline axis (Fig. 4b and 9c). There the BRGM found two main NGM deposits here, along the Aron and Gras rivers, which contained 1150 t and 800 t of grey monazite respectively. These alluvial deposits are primarily composed of clay, silt, sand and gravel beds. Heavy monazite grains mostly consist of grey nodules that occur in a basal gravel unit over a thickness in the range of 1 m and a total area extent of 20 km long for 35 m width. The concentration ranged between 400 and over 5 000 g of monazite per m^3 of gravel (*i.e.* ≈ 160 to >2000 g/t, Fig. 9c) at different exploration sites, with an average grade of about 2000 g of monazite per m^3 of gravel (*i.e.* ≈ 800 g/t). The BRGM produced 78 t of monazite concentrate from 1967 to 1968, operating La Monnerie placer deposit on a pre-industrial pilot scale (Fig. 9d, e). Although these exploration activities were focused on placers, they also provided some data on the average monazite content in shales (Fig. 9c). These works (Guigues and Sapinart 1967) also highlighted that

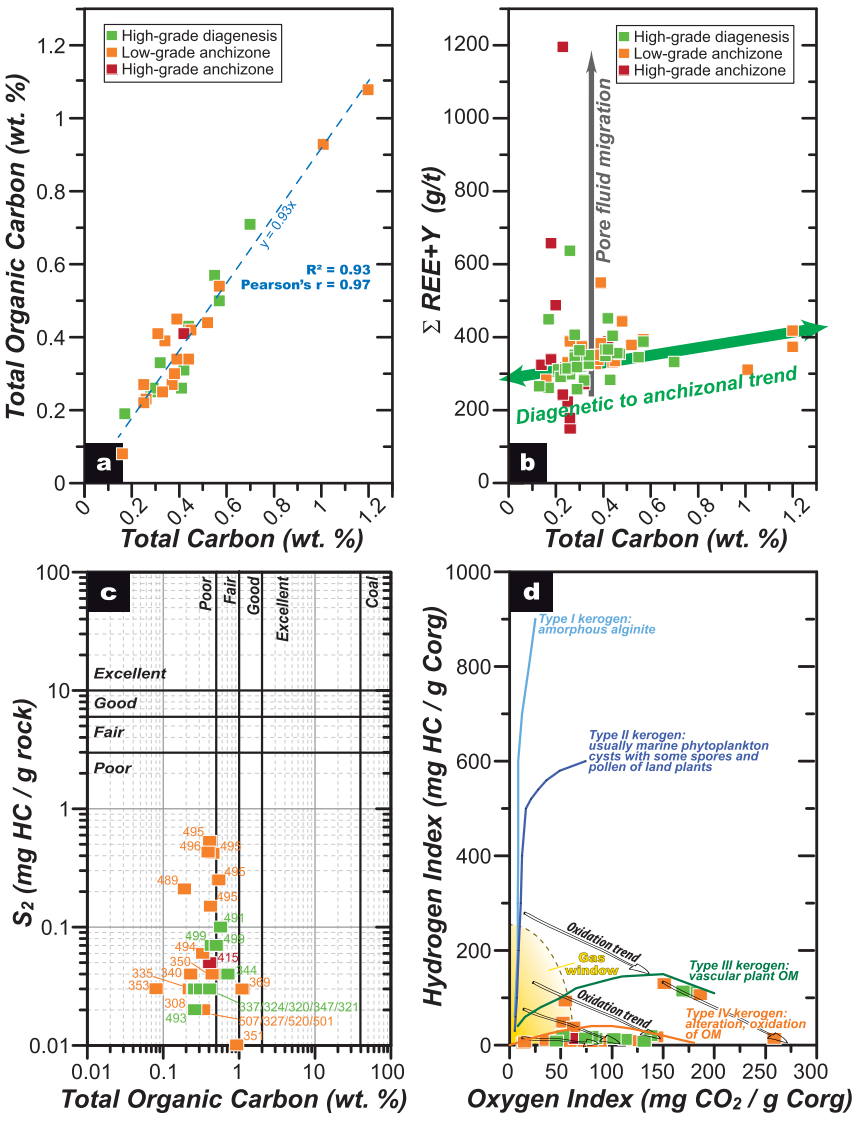

Fig. 8. a) Total organic carbon from rock-eval method (toc) versus Total Carbon (TC). b) Distribution of samples in a REE + Y versus TC diagram. c) Plot of the amount of hydrocarbon (HC) formed during thermal decomposition of the kerogen (S2 parameter) versus TOC. The Tmax value, a Rock-Eval maturity indicator, is shown for each sample. d) Shale samples plotted on a pseudo-Van Krevelen diagram. Data are presented with respect to their provenance in both the Angers-Traveusot and the upper part of the Grés Armoricain Formations (high-grade diagenesis, low- and high-grade anchizone domains, as in Fig. 5b). OM: organic matter.

monazite-rich beds are correlated with fossiliferous and organic-rich layers (Fig. 8b, 9c and 10a). In addition, the monazite distribution within the sedimentary rocks is not equal across the whole area (Fig. 9c). The exploration works showed that the richest sites are located in the lower third of the Angers-Traveusot Formation, particularly along the Glévardais – Pont des Iles anticline axis, where the average monazite content is about 200 g/t (*i.e.* > 130 g of REE per t of shale; Lulzac, 1969). This explains the exceptional enrichment of alluvial placers in this area. It should be noted, however, that we find different values to those of prospectors, with a median value for our REE + Y concentrations in shales close to 340 g/t, *i.e.* roughly equivalent to 500 g of equivalent monazite per t of shales. These calculations of monazite per ton of shale are based on the assumption that all REE + Y occur in the monazite and that there is a 100% recovery rate during crushing, sifting and heavy mineral separation, regardless of grain size. Given that the prospecting activities recovered a grain size fraction of between 0.2 and 1.5 mm, the smaller-sized grains we identified would reduce the recovery rate, even assuming that monazite is the only REE-bearing phase.

Study of thin sections from rock samples, as well as polished sections of monazite concentrate from La Monnerie placer reveals three different generations of monazite, all observed in the Angers-Traveusot and the upper part of the Grès Armoricain formations. Detailed information on monazite chemistry can be found in Supplementary Appendixes 5 and 6.

Type 1 consists of typical NGM that forms elongate shapes, from sub-microscopic size to ca. 1.5 mm. Such nodules are by far the most abundant REE-phase in the shales and occur only in anchizonal rocks. It means they are found in both the low-grade anchizone of the Angers-Traveusot Formation where they are widespread, and in the underlying rocks of the high-grade anchizone such as at Le Pont d'Aron. Elongate nodules tend to develop parallel to the bedding (Fig. 10a and b). The nodules exhibit a porous structure and display a distinctive texture characterised by abundant inclusions of various minerals. These inclusions are made of phyllosilicates, quartz, feldspar, rutile, graphite and iron oxides, with sizes reaching *ca.* 15 μm in size (Fig. 10b), and constitute up to about 20% of the nodule's composition. Raman analysis of several nodules failed to reveal the presence of rhabdophane (hexagonal $[LREE]PO_4 \cdot H_2O$), as previously suggested by Donnot et al. (1973). Some nodules have developed a chlorite-rich mantle that can form symmetric tails as described in exploration works. Type 1 NGM has a heterogeneous chemical composition, which can be used to distinguish end-member compositions. Grains over 250 μm in size show typical core-rim chemical zoning (Fig. 10c), whereas smaller grains (≪200 μm) have no chemical zoning; and instead show a complex assemblage of sub-micrometric monazite proto-aggregates (Fig. 10f-g). Nodule cores typically have either a monazite-(Nd) to monazite-(Ce) composition whereas all rims have a monazite-(Ce) composition (Fig. 11a). The LREE

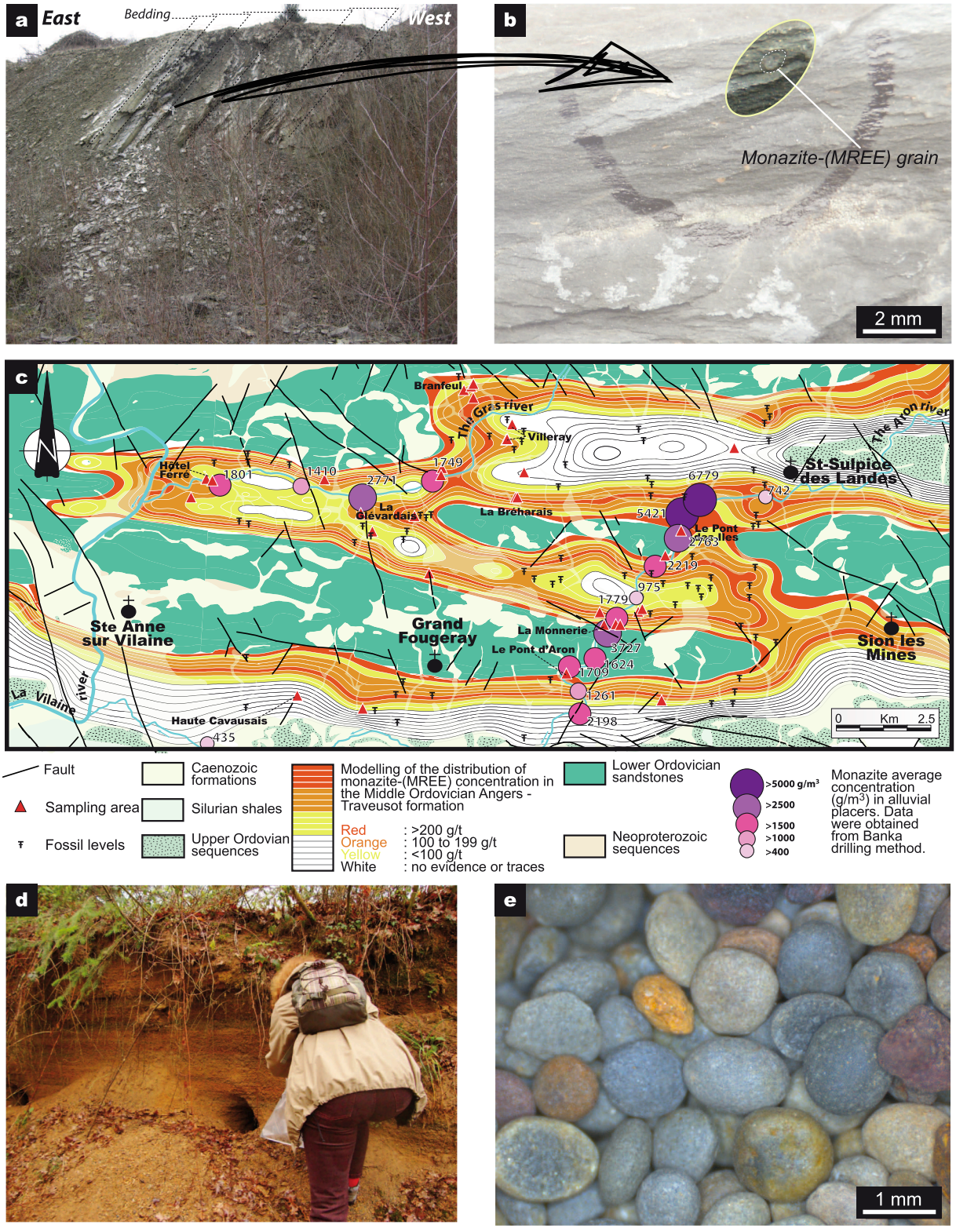

Fig. 9. Outcrop conditions of grey monazite nodule occurrences a) La Bréharais quarry, and b) a large grey monazite nodular grain. Note that this occurrence is located along the fertile northern limb of the Glévardais – Pont des Iles anticline axis. The bedding strikes roughly E-W and dips to the north at approximately 40°. c) Modelling of the distribution of the monazite nodule content in g/t within the Middle Ordovician Angers-Traveusot Formation. This is an interpolation of previous exploration data (Lulzac, 1969) with our potential-field interpolation method in which the shale formation has been separated into 18 stratigraphic sequences. Monazite concentration in alluvial placers noted in previous exploration works (Guigues and Sapinart, 1967) is divided into 5 different grades and expressed in g/m3 of gravel. d) Remaining monazite-rich sands from La Monnerie placer deposit operated between 1967 and 1968. e) Nodular grey monazite concentrate obtained from monazite-rich sands from La Monnerie.

contents of the largest nodule cores are highly variable in terms of Nd, Ce and La (15.7 to 23 wt% with $\overline{X}$ = 19.4 wt%; 15.8 to 24.5 wt% with $\overline{X}$ = 20.8 wt% and 3 to 7.6 wt% with $\overline{X}$ = 5.1 wt% respectively), and less for Pr (3.1 to 4.3 wt% with $\overline{X}$ = 3.8 wt% Pr, Fig. 11a-d). Relatively high values of Sm (up to 9 wt% with $\overline{X}$ = 5.2 wt% Sm) with moderate Gd (up to 4.2 wt% with $\overline{X}$ = 2.5 wt% Gd) and Eu (up to 1.1 wt% with $\overline{X}$ = 0.7 wt % Eu) is also a characteristic feature of the type 1 NGM cores (Fig. 11e). Note that smaller grains are similar in composition to certain cores, being enriched in Pr and having a typical monazite-(Nd to Ce) core composition (Supplementary Appendix 5). Because of these strong textural and compositional similarities, we assume that both textural assemblages underwent the same paragenesis. We have thus incorporated the small monazite grains into type 1 NGM cores in the figures. This raises questions as to the growth model of grey monazite nodules. We suggest an aggregation model favouring high saturation and nucleation rates rather than the growth of a nanocrystal, as reported for framboidal pyrite (Wilkin and Barnes, 1997). Note that both Ce and La contents increase toward monazite-(Ce) rims (Fig. 11a and b) whereas Nd content shows a negative correlation (Fig. 11a and d). The LREE contents of the nodule rims show marked enrichment in Ce and La and a Nd depletion (22.8 to 29.6 wt% with $\overline{X}$ = 26.4 wt%; 5.6 to 18.9 wt% with $\overline{X}$ = 10.4 wt% and 18.7 to 8 wt% with $\overline{X}$ = 13.4 wt% respectively, Fig. 11a-b, d). The Pr content also varies with the core-rim chemical zoning as it increases gradually in core grains, whereas it decreases gradually in rims (Fig. 11c). The Pr content (Fig. 11c) suggests that core compositions are positively correlated with La and Ce, whereas they are negatively correlated in the rims. The Sm, Gd and Eu values are low in grain rims (up to 3.9 wt% with $\overline{X}$ = 2.3 wt% Sm; up to 2 wt% with $\overline{X}$ = 1.2 wt% Gd, and up to 0.3 wt% with $\overline{X}$ = 0.3 wt% Eu, Fig. 11e). The Y content is variable but generally low (up to 0.7 wt% with $\overline{X}$ = 0.4 wt% Y) and no clear trend has been observed with respect to core – rim chemical zoning. The Th and U contents are also low, ranging from a few hundred or tens of ppm to 1.5 wt% and 600 ppm respectively (Fig. 11f). Again, no clear distribution has been observed with respect to core – rim chemical zoning. Note that EPMA mapping reveals a significant clustering of Th in the grain rims (Fig. 10c).

By contrast, type 2 monazite is rare and occurs in the high-grade anchizone. It consists of anhedral grains, with rare inclusions and is characterised by replacement-recrystallization textures of type 1 NGM (Fig. 12a, b), possibly due to dissolution. Grains typically have a monazite-(Ce) composition (Fig. 11a), and show the highest enrichement in both Ce and La (23.7 to 29.2 wt% and 9.2 to 22.1 wt% respectively), while being depleted in Nd and Pr (7.6 to 13.4 wt% and 2.3 to 3.7 wt% respectively, Fig. 11a-d). They also have the lowest concentration of MREE, with a low Sm content (up to 1.8 wt%), and almost negligible Gd and Eu contents (up to 1.1 and 0.4 wt% respectively, Fig. 11e). The U and Th contents are also low, with maximum at 480 and 5900 ppm respectively (Fig. 11f). This type 2 monazite-(Ce) paragenesis may be related to chlorite.

Type 3 monazite is common (Fig. 12c-f) and is always found in association with chlorite. It occurs in the low-grade anchizone domain, and also very rarely in the high-grade diagenesis at Hôtel Ferré, where grains are associated with xenotime. (Fig. 5c). Type 3 monazite grains are associated with veinlets/fractures (<1mm) that may develop a discrete halo of chlorite (Fig. 12c, e, f), occurring either within the veinlets or in the alteration halo. Xenotime, on the other hand, was only observed in the alteration halo. The veinlets themselves are composed of a quartz and/or chlorite assemblage. The type 3 monazite grains have a heterogeneous chemical composition (Fig. 11) that ranges from the monazite-(Nd)-(Ce) boundary to clearly monazite-(Ce). Grains within the veins tend to have a marked monazite-(Ce) composition (Fig. 11a), while those in the halo are similar to type 1 NGM cores, with enrichment in Pr, Nd, Sm or Gd, for instance, but La depletion (Fig. 11b-e). Note that monazite found in fractures has lower U and Th values (up to 204 and 4082 ppm with $\overline{X}$ = 119 and 2014 ppm respectively) than those in chlorite haloes (up to 225 and 4790 ppm with $\overline{X}$ = 169 and 3318 ppm respectively, Fig. 11f). Type 3 monazite exhibits the highest degree of variability in Y content, ranging from levels below detection (or 0) to approximately 0.4 wt% with $\overline{X}$ = 0.15 wt% Y. This variability probably arises from its unfavourable partition coefficient compared to xenotime. When in equilibrium with type 3 monazite, xenotime can contain as much as 32 wt% Y. It is typically depleted in LREE and enriched in MREE.

Monazite chemical zoning is well-illustrated in the UCC-normalized REE patterns (Fig. 13). The REE pattern of type 1 NGM cores mimics a right-skewed bell-shape with a maximum at Sm (Fig. 13a). Type 1 NGM rims are enriched in La and Ce and depleted in Pr to Dy with respect to type 1 NGM cores. Note that rim patterns have a relatively flat spectrum for LREE and MREE with either a negative Sm anomaly or positive Eu anomaly. Type 2 monazite-(Ce) shows a pattern with a decreasing content from La to Gd, and a slightly positive Eu anomaly (Fig. 13b). Like type 2 monazite-(Ce), type 3 monazite-(Ce) found in veinlets mimics the type 1 NGM rim pattern (Fig. 13a-c), while type 3 monazite-(Nd-Ce) found in chlorite haloes has patterns that lie between type 1 NGM rims and cores (Fig. 13a, c). The coupling of the geochemical twins Y and Ho (termed CHARAC; CHArge- and RAdius-Controlled) for all monazite types suggests a non-CHARAC behaviour probably due to a specific chemical complexation with a wide variety of ligands in the exogeneous medium and/or to their adsorption on mineral surfaces (Bau, 1996).

4.5. *Monazite U/Pb geochronology and U, Th, Pb content of monazites*

Although the in-situ U–Pb monazite dating method is highly sensitive, age determination of NGM was challenging because of the combination of abundant host-rock inclusions and compositions with low U content and significant non-radiogenic Pb content. In order to increase the number of usable analyses, we chose to lower the detection limits by increasing the beam size from 10 to 15 μm, thus enlarging the sample volume but reducing the number of suitable areas that contained a low percentage of mineral inclusions and porous defects. Analyses with the lowest U (and radiogenic Pb contents) below detection limits, were not carried through our data processing and only those above were kept for age determinations. Seventy-nine analyses were performed on four large monazite grains (L2G7, L3G7, L4G9 and L5G3) from the La Monnerie heavy concentrate (Supplementary Appendix 6) mounted on a polished section. Grain sizes ranged between 600 and 1500 μm, with typical type 1 NGM core and rim zoning and porous / inclusion-rich texture (Fig. 12a, b). Grains L2G7 and L5G3 also show replacement features of type 1 monazite-(Nd) by type 2 monazite-(Ce), the latter being almost inclusion-free (Fig. 12a, b). Twenty-two analyses were carried out on monazite grains from two polished thin sections (GF11-13 and GF12-04). Grains in GF12-04 have type 1 NGM features and range in size from 200 to 400 μm. Monazite from GF11-03 consists mainly of type 3 monazite-(Ce) filling fractures (Fig. 12c, d). No dating was completed on xenotime grains because of their small size and scarcity.

The combined measured U-Pb data are plotted in a Tera-Wasserburg diagram (Fig. 14). The analyses are mostly discordant reflecting the incorporation of various amounts of common-Pb, but form a clear alignment (Fig. 14). The Th, U and Pb contents are low in all monazite types. Th concentration is the most heterogeneous and ranges from 293 to 9252 ppm ($\overline{X}$=1861 ppm). These data are consistent with the limited values obtained by EPMA. The U and Pb contents are similar and positively correlated, varying from 17.8 to 479 ppm ($\overline{X}$=127 ppm) for U and 19.4 to 1042 ($\overline{X}$=1571 ppm) for Pb. Based on textures and chemical composition, three U-Pb age groups can be identified.

i) Age group 1 was obtained for both cores and rims of type 1 monazite, which show variable Th/U ratios of between 1.6 and 79.6 (average value of 14.4). Core and rim ellipses are well

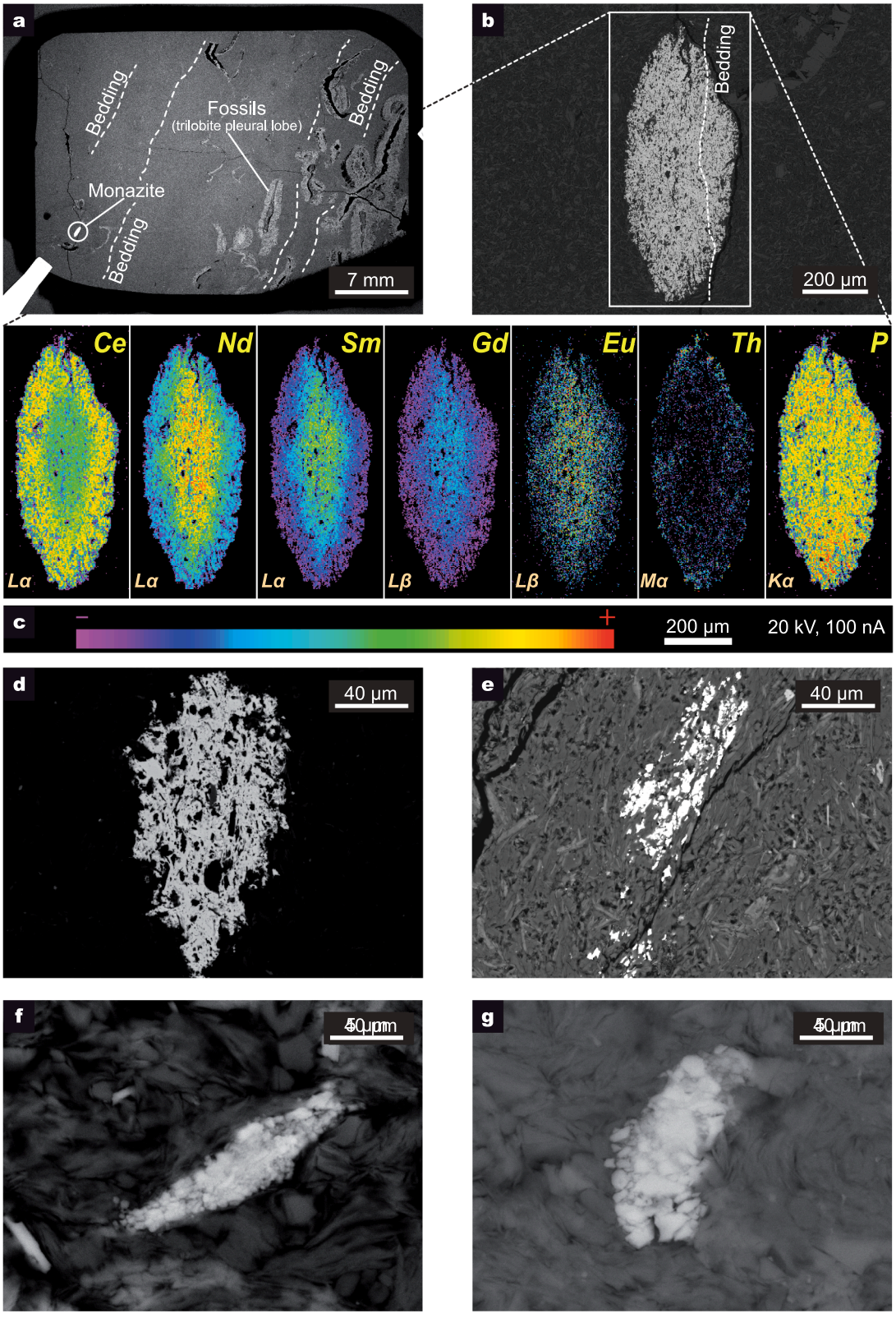

Fig. 10. Type 1 nodular grey monazite and small monazite grain geochemistry. a) Backscattered electron image of a thin section of a monazite nodule within a fossiliferous and TOC-rich shale. Sample GF12-06 from Branfeul. b) Backscattered electron image of a large monazite nodule. Note the thin bedding parallel to the grain and the porous texture. Sample GF12-05 from Branfeul. c) Electron probe micro analyser (EPMA) mapping of monazite nodule for Ce, Nd, Sm, Gd, Eu, Th and P. Sample GF12-05 from Branfeul. Backscattered electron images of small monazite grains from Branfeul d) sample GF12-05 and e) sample GF12-06, f and g) Cherhal (sample GF11-04).

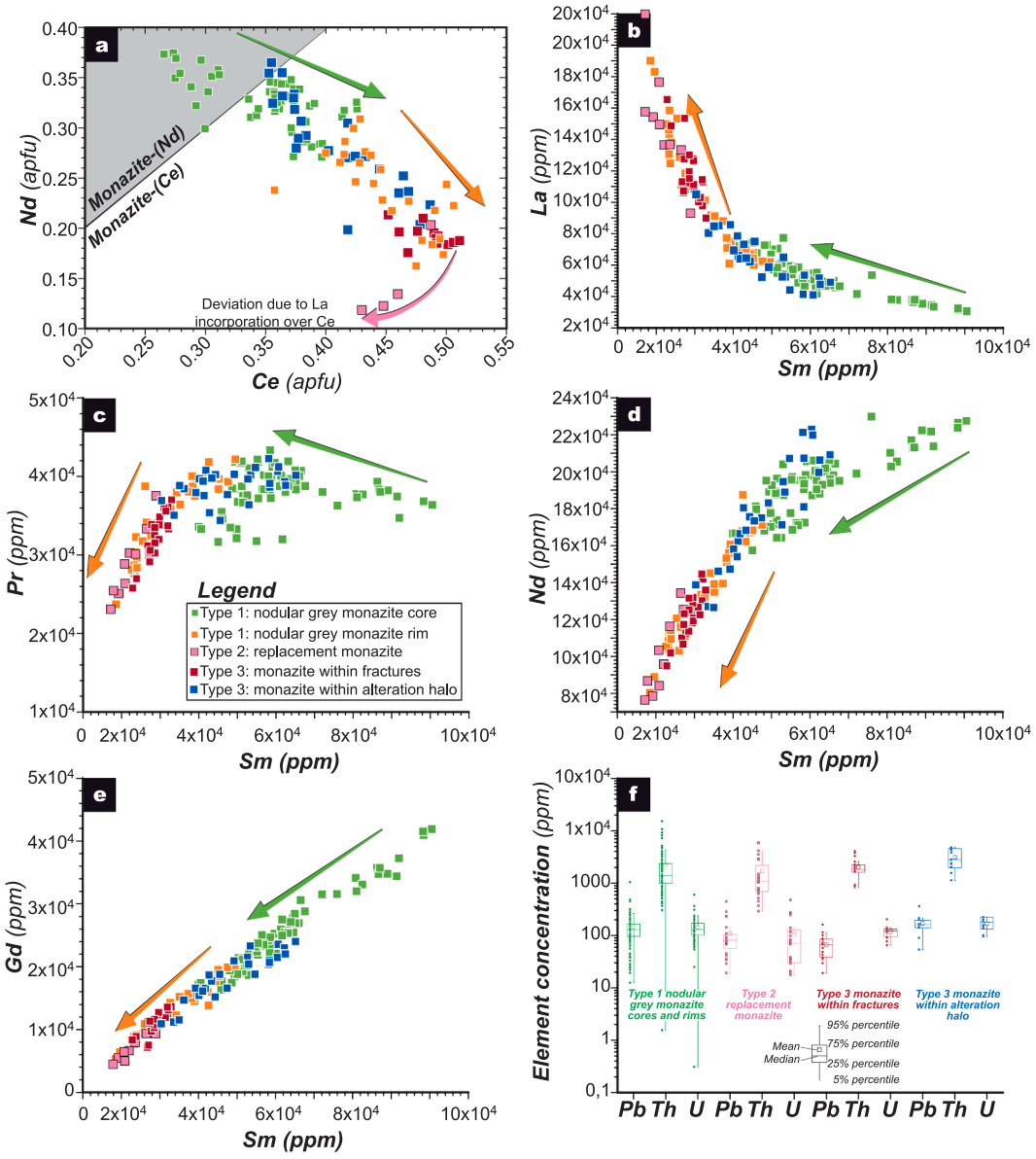

Fig. 11. Diagrams showing variations in La, Ce, Pr, Nd, Sm, Gd, Pb, Th and U contents in monazite grains. a) Monazite end-member composition with respect to Nd and Ce content. Note that elements are in atoms per formula unit (apfu).Variation diagrams depicting the amount of b) La, c) Pr, d) Nd, e) Gd with respect to Sm. Legend is given in c and element concentrations are in ppm. f) Box plot graph illustrating the Pb, Th and U contents for all monazite types. Because there is no difference between type 1 monazite cores and rims, the data were merged.

aligned and yield an age of 403.6 ± 2.9 Ma (MSWD[1] = 1.0; p(χ^2) = 0.5, Fig. 14a).

ii) Age group 2 consists of replacement type 2 monazite-(Ce). Th/U ratios are also heterogeneous with an average value of 10.7, and min. and max. values of 0.6 and 59.6 respectively. The 19 analyses give an age of 382.6 ± 6.9 Ma (MSWD = 1.6, p(χ^2) = 0.1, Fig. 14b).

iii) Age group 3 consists of type 3 monazite-(Ce) observed in veins and fractures. Th/U ratios are low with an average value of 10.9, similar to type 2, and min. and max. values of 3.5 and 20.6 respectively. Intersection of the regression line with the Concordia gives an age of 349.6 ± 6.0 Ma (MSWD = 1.1, p(χ^2) = 0.4, Fig. 14c).

5. Discussion

5.1. Timing of the low-grade metamorphic event: A pre-Variscan geological setting

The KI variations show that sedimentary rocks from the Grand Fougeray area underwent very low-grade metamorphic conditions ranging from high-grade diagenesis and low-grade anchizone in the Angers-Traveusot Formation to the high-grade anchizone in the upper part of the Grès Armoricain Formation. Epizone conditions are assumed to have occurred in the underlying Lower Ordovician and basement formations according to Le Corre (1975). Clays are dominated by smectite in the diagenesis domain, and illite in the anchizone. Note that, in the Grand Fougeray area, the conditions are generally consistent with those proposed by Le Corre (1975). He suggested a N080°E trending regional metamorphic thermal anomaly possibly related to a hidden plutonic intrusion. According to Gapais and Le Corre (1980), and

[1] MSWD: mean square of weighted deviation.

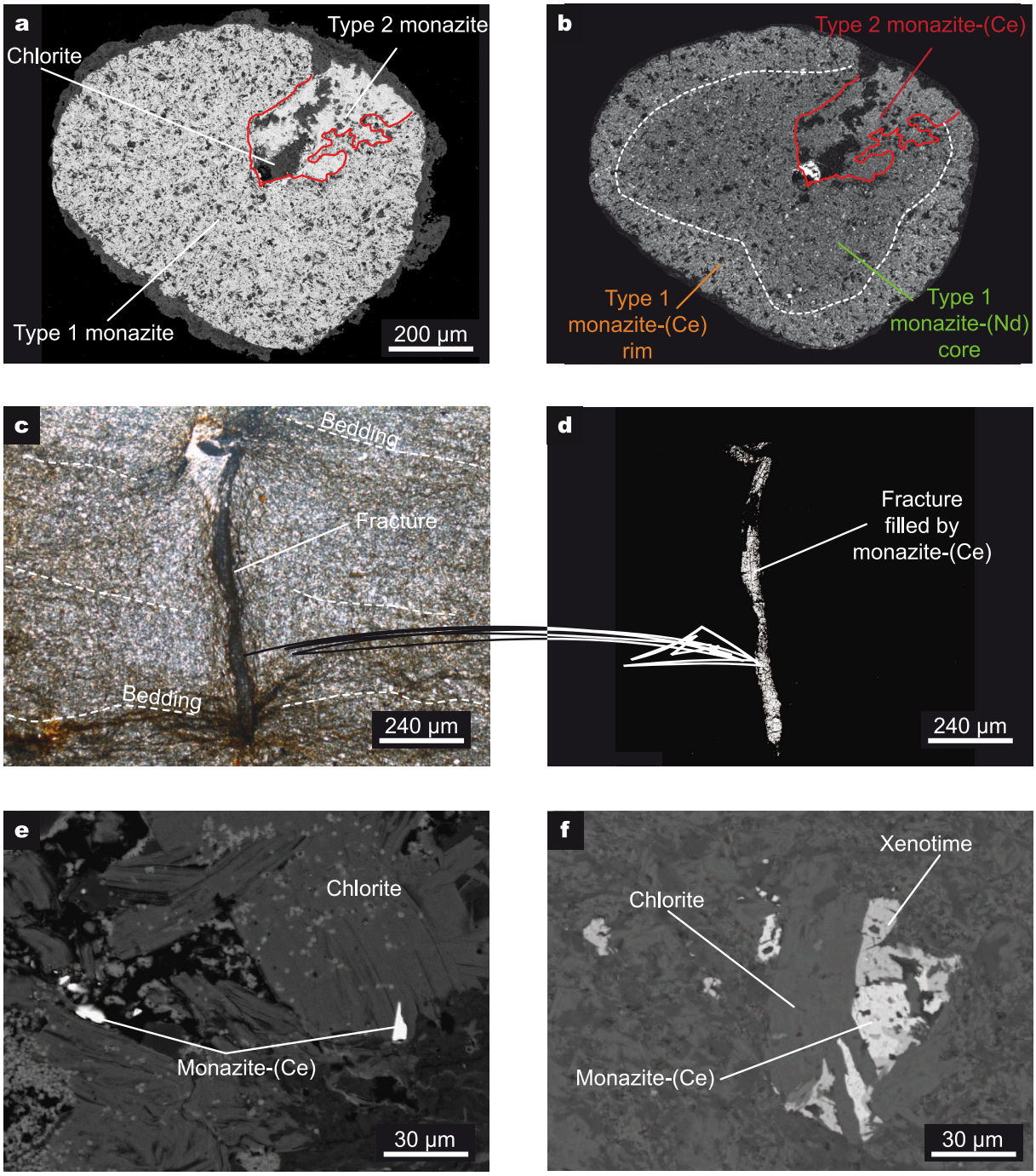

Fig. 12. Monazite geochemistry. a) Backscattered electron and b) cathodoluminescence imaging of a heavy grey monazite grain from alluvial placers showing type 1 monazite-(Nd) core and monazite-(Ce) rim compositions, as well as narrow re-entrant "corrosion" features filled with type 2 monazite-(Ce) and chlorite. Note the porous texture. The dark grey assemblage that rims the nodule corresponds to the remnant quartz-clay mineral ± chlorite matrix from the shale host-rock. Grain L5G3 in polished section, same scale. c) Plane polarized light microscopy of vein/fracture discordant to the bedding and, d) filled by monazite-(Ce). Backscattered electron image, sample GF11-13 from Gras Richomme. e) Backscattered secondary electron image of a small monazite-(Ce) grain within chlorite sheets. Sample GF12-13 from Gras Richomme. f) Backscattered secondary electron image of a thin section depicting monazite, xenotime and chlorite paragenesis. Sample GF11-08 from Hôtel Ferré.

Gumiaux et al. (2004), the bedding and cleavage define an upright fold system with ca. N110°E-trending fold axis. No clear correlation can be made between the metamorphic gradient distribution and the distance to the northern branch of the South Armorican Shear Zone, *i.e.* there is no clear increase in metamorphic gradient toward this major shear-zone. Similarly, no correlation has been made between the metamorphic gradient distribution and the presence of a granite body at depth including along the N080°E trending direction. Based on the 2D modelling of the folding in the Angers-Traveusot Formation using the potential-field interpolation method and its intersection with a flat plane (giving a difference in height between the highest and lowest point of max. 50 m, Fig. 5c), we show that metamorphic isograds follow the stratigraphic sequence and are folded too. The Angers-Traveusot Formation thus reached its peak metamorphism prior to the Variscan folding event, possibly during burial of the basin sequences.

KI can be used to approximate temperature ranges for metamorphic

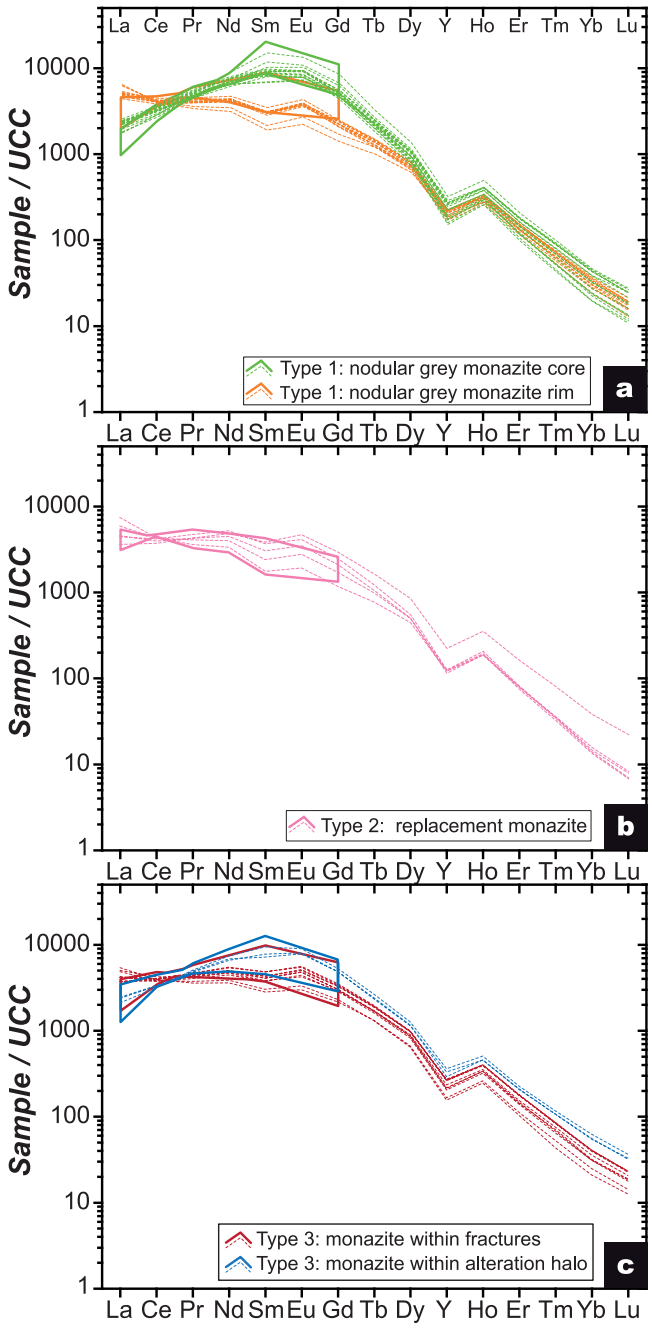

Fig. 13. UCC-normalised REE patterns for: a) type 1 monazite nodule cores and rims, b) type 2 replacement monazite, and c) type 3 monazite found both in veins and alteration haloes. UCC values are from McLennan (2001). Dotted lines correspond to LA-ICP-MS analyses, while polygons correspond to EPMA data.

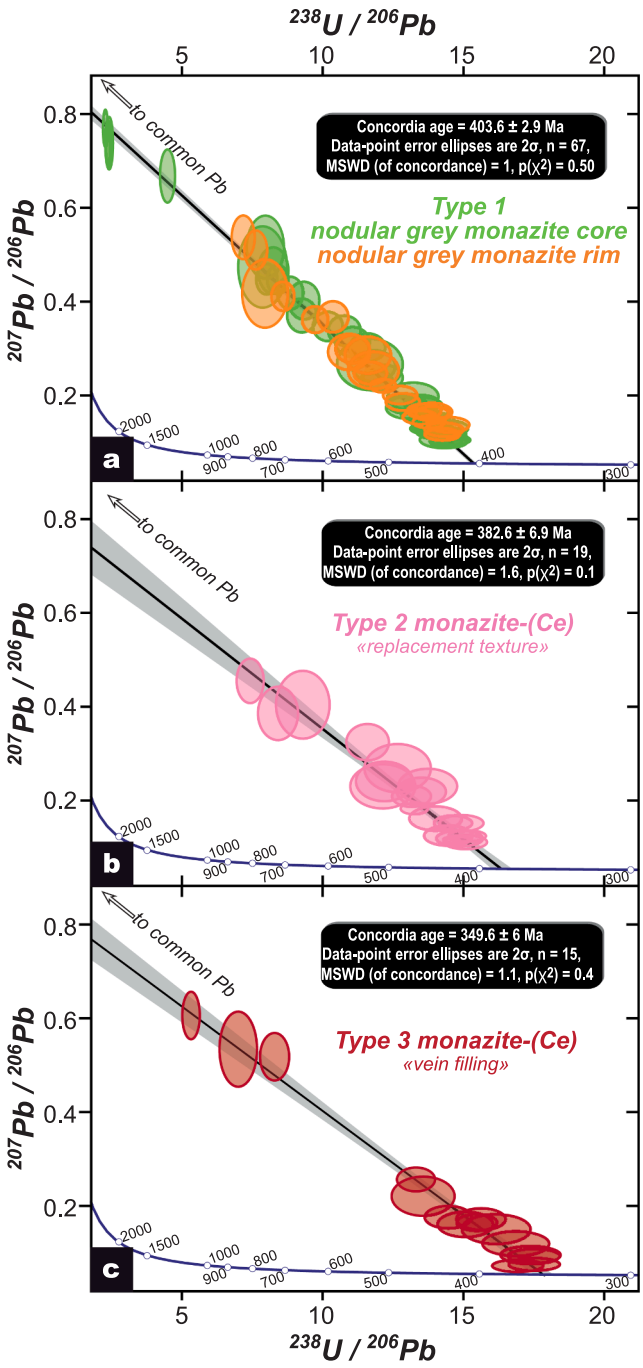

Fig. 14. U–Pb analyses for monazite grains. Tera & Wasserburg (1972) Concordia age is calculated using the concordant data. Samples that lie off the concordia line are aligned along discordia lines and form isochrons for: a) type 1 nodular grey monazite-(Nd / Ce) cores and rim overgrowths, b) type 2 monazite-(Ce) displaying recrystallization-replacement textures on type 1 nodular grey monazite, and c) type 3 monazite-(Ce) in veins. MSWD, mean square of weighted deviation; p(χ2) mean Pearson's chi-squared test.

conditions (Frey, 1987; Ferreiro Mählmann, 2001; Merriman and Frey, 1999; Potel et al., 2006, Zhu et al., 2016). The temperature is approximately 215 °C for the high-grade diagenesis / low-grade anchizone boundary, 250 °C for mid-anchizone, and above 300 °C for the high-grade anchizone / epizone transition (Fig. 5a). From bottom to top, the Lower Ordovician sedimentary rocks (*i.e.* the Pont-Réan and Grés Armoricain formations) that occur in the Grand Fougeray area underwent epizone to upper anchizone metamorphic conditions (this study and Le Corre, 1975). The average temperature recorded in the upper part of the Grès Armoricain Formation is 264 ± 16 °C at Le Pont d'Aron (calculated from Zhu et al. (2016) equation). The overlying Angers-Traveusot Formation was affected by lower metamorphic grades, with the lower one-third characterised by lower anchizone metamorphism (temperatures between *ca.* 215 °C and 250 °C, $\overline{X}$ = 227 ± 7 °C), and the upper two-thirds by high-grade diagenesis (temperatures lower than *ca.* 215 °C, $\overline{X}$ = 170 ± 23 °C). The high-grade anchizone boundary thus roughly coincides with the contact between the upper part of the Lower Ordovician Grès Armoricain and the Middle Ordovician Angers-Traveusot formations (Fig. 5c).

5.2. Diagenetic evolution and processes for nodular grey monazite formation

In the Grand Fougeray area, the HC content of the Angers-Traveusot Formation is quite low (Fig. 8c), and in the pseudo-Van Krevelen diagram (Fig. 8d), samples cluster within the type IV and more rarely type III kerogen fields. Because vascular plants are considered to have originated and adaptively radiated only from the Silurian Period (Gensel 2008), a type III origin for the OM is precluded. This strongly reinforces the hypothesis that the OM has undergone periods of severe alteration and oxidation. It is reasonable to assume the original OM was at least fairly abundant, marine (*i.e.* phytoplankton) and terrestrial (e.g. spores) in origin. We therefore suggest that type II kerogen underwent substantial oxidation during and after the thermal maturation as suggested by the oxidation trends with a negative slope (Fig. 8d). Samples with a low Oxygen Index ($\ll$50 mg CO_2/g C_{org}) can be interpreted as the least altered. The Angers-Traveusot Formation is inferred to be composed of over-mature sediments that had been oxidised just prior to, as well as after reaching the gas generation stage (Fig. 8d). According to Pepper and Corvi (1995), such a gas generation window would be effective in the high-grade diagenesis domain at temperatures lower than 220 °C for dominantly marine organo-facies. Note that such a temperature range roughly coincides with the transition from the diagenesis domain to the anchizone.

In siliciclastic sedimentary rocks, K occurs mainly in K-feldspar, mica and clay minerals both of detrital and diagenetic origin. The distribution of Rb, and K in grains of different sizes depends on the maturity of the sediment: in immature sediments both elements are equally distributed throughout all grain sizes, whereas in mature sediments, they are carried predominantly by clay minerals in the finest fraction (Matys Grygar et al., 2019; van de Kamp, 2016; von Eynatten et al., 2016). In Fig. 7a, most samples with low K/Al (0.08–0.32) and K/Rb (140–190) ratios belong to the diagenetic and low-grade anchizone domains that plot within the Holocene and Pleistocene mud fields. According to Van de Kamp (2016), this suggests that the shales have been maintained and undergone evolution under the effects of isochemical diagenetic processes, thus limiting K-metasomatism. Evolution of rock sample compositions may lead to higher K/Al (0.26–0.40) and K/Rb (170–220) ratios (Fig. 7a), such as for some samples of the high-grade anchizone (*i.e.* from the upper part of the silty-clay Grès Armoricain Formation), and a few localities belonging to the low-grade anchizone and high-grade diagenesis. These sedimentary rocks may have been altered and subject to K-metasomatism in an open system. The main K-bearing phases in all samples are clays, particularly illite. According to Vidal and Dubacq (2009), clay dehydration processes involve large and sudden volume changes related to water release and the loss of H_2O layers, and occur in successive incremental steps during the burial of sediments. The greatest loss (~65 mol %) of water occurs between 40 and 220 °C during which three breakdown reactions have been identified by modelling. The two first steps are assumed to take place under early diagenetic conditions (<120 °C). The third occurs at the boundary between the diagenetic domain and the anchizone, at around 200–220 °C, and results in the release of 26 mol % water. Dehydration reactions continue at higher temperatures although water release is much lower. We may thus assume the high-grade diagenesis to low-grade anchizone diagenetic processes imply in-source fluids released in response to clay dehydration reactions.

While the overall concept of NGM growth resulting from burial, increased temperature and fluid generation is reasonably well accepted (e.g. Burnotte et al., 1989; Milodowski and Zalasiewicz, 1991; Rasmussen and Muhling, 2007), the sources of REE and P, and the reactions which might produce authigenic NGM under conditions of very low-grade metamorphism are not clearly understood. They may be related to: i) desorption of REE adsorbed on the surface of clay minerals during their diagenetic transformations (Burnotte et al., 1989; Milodowski and Zalasiewicz, 1991; Rosenblum and Mosier, 1983); ii) desorption of REE and P during early diagenetic reduction of Fe oxides/hydroxides (Lev et al., 1998; März et al., 2008; Yang et al., 2017); iii) degradation of OM (REE sorbed onto the surface coatings or incorporated into biogenic material) in response to early burial compaction (Evans and Zalasiewicz, 1996; Lev et al., 1998; März et al., 2008; Yang et al., 2017); and iv) dissolution of detrital REE-minerals including monazite as has been described for greenschist-facies metasediments (Janots et al., 2008; Rasmussen and Muhling, 2007). It should be noted that clays in siliciclastic fractions preferentially sorb HREE (including Y) over LREE (Coppin et al., 2002). Similarly, sediments entering the gas window are assumed to release more HREE from OM (Yang et al., 2017). Hence, the ongoing dehydration processes affecting clays and the OM maturation are assumed to release both water and the refractory HREE + Y into micropores at the end of diagenesis during the methanogenesis stage.

We do not find any evidence that clearly supports one hypothesis more than another. In fact, NGM probably form in response to these different competing influences. Note that despite the low OM content in the Angers-Traveusot Formation (0.1 to 1.1 wt% TOC; $\overline{X} = 0.4 \pm 0.2$ wt %), both the REE + Y and TOC contents present interesting correlations (Fig. 8b, 9c), and the NGM occurrences do not preclude OM having been an important REE (and P) source. Indeed, these sedimentary rocks generally have a high REE + Y content (Fig. 8b) with average concentration close to 340 g/t, which increases slightly, together with the OM content, up to 450 g/t in the absence of alteration, *i.e.* twice that of NASC and ES (McLennan, 1989). This is reinforced by the fact that both TOC and H (S_2 parameter) decrease during sediment burial proportionately to the amount of reactive kerogen that is consumed (Fig. 8d). As thermal processes control OM maturation, clay transformation and fluid generation, NGM distribution may be controlled by burial as well as being dependent on the metamorphic isograd distribution.

In terms of the thermomechanical properties of the Angers-Traveusot Formation, shales are known to have very low permeability due to their very fine grain size, which prevents or strongly limits both fluid migration and infiltration. This property may explain the rather constant ΣREE + Y and TOC contents (Fig. 7e, 8b) and the isochemical evolution of the majority of the formation (Fig. 7a). This means that REE, Y and P released during the burial of the sediments have undergone limited or no migration within the shale formation. This also raises the question as to whether the now-oxidised Angers-Traveusot Formation, was in fact a former oil- or gas-shale. We can assume that NGM nucleation was enhanced by desorption and dehydration steps that led to a progressive enrichment in REE and P in the shale's pore space. Alteration may have occured locally, which could be explained by fracturing and upward fluid migration. Where the Angers-Traveusot Formation is altered and has undergone fluid migration processes (Fig. 7a), the REE + Y content is heterogeneous and ranges from 175 to 1200 g/t (Fig. 8b) particularly in the upper anchizone part. It should be noted that metasomatism is essentially confined to the rocks belonging to the upper part of the Grès Armoricain Formation, which mostly consist of higher permeability sandstone and silty-clay formation.

5.3. Origins and timing of monazite formation

All the monazite occurrences are situated in the anchizone domain, with one exception for a type 3 monazite-xenotime assemblage, which occurs in the high-grade diagenetic domain at Hotel Ferré. NGM is by far the most abundant REE-phase in shales. Likewise, the source of heavy NGM grains in streams must be derived from weathered and eroded anchizonal shales, given that the diagenetic ones are almost devoid of NGM.

Type 1 NGM consists of typical nodules with irregular to ovoid elongate shapes up to 1.5 mm (Fig. 10). They are characterised by a porous texture in which numerous small mineral inclusions occur such as the ones observed in the surrounding shales. This textural evidence precludes a detrital origin and suggests an authigenic origin (Donnot

et al., 1973; Burnotte et al., 1989). Moreover, the lack of detrital cores and altered detrital monazite means that the NGM cannot be derived from fluid-assisted dissolution of detrital metamorphic monazite. Type 1 NGM grain zoning is complex and reveals a core enriched in MREE (and Nd) and rims in LREE (mostly Ce and La). NGM grains have MREE-enriched UCC-normalised patterns (Fig. 13a), although the grain cores have higher MREE concentrations than the rims. Considering the low permeability of the shale formation, NGM formation depends on both REE and P evolution in the pore fluid during burial and on low-grade diagenetic to very low-grade metamorphic conditions. Indeed, a bell-shaped REE + Y pattern has been observed in diagenetic fluids, and intensive P, LREE and MREE liberation into sedimentary pore waters, and redistribution attributed to diagenetic processes has been described for terrigenous sequences (Evans et al., 2002; Haley et al., 2004; Johannesson and Zhou, 1999; Kim et al., 2012; Lev et al., 1998; Milodowski and Zalasiewicz, 1991; Janots et al., 2008). The main controlling factor for such processes is the redox conditions (Dabard and Loi, 2012; März et al., 2008; Yang et al., 2017). The terrigenous Angers-Traveusot Formation corresponds to an outer shelf depositional environment (Henry, 1989) where anoxic conditions are quickly attained, preventing extensive phosphogenesis (apatite crystallization; Dabard and Loi, 2012; Jarvis, 1994). Under such oxygen-free conditions, OM maturation takes place via reactive reduction of Fe-oxyhydroxides, a process that releases both P and REE into pore fluids (Freslon et al., 2014; Haley et al., 2004; März et al., 2008; Yang et al., 2017). Because compaction gradually reduces sediment porosity during burial, pore fluids have increasing difficulty migrating upward. We therefore assume that NGM likely formed in response to the desorption and dehydration processes cited above, leading to the progressive enrichment in REE and P in shale pore waters, with MREE enrichments from OM, Fe-oxyhydroxides and clays. When buried shales reach the high-grade diagenesis - anchizone transition, the ongoing release of REE + Y and P leads to monazite saturation, in the absence of CaO which prevents apatite precipitation. Such low Ca contents with values below 0.5 wt% CaO, are also typical for schists containing authigenic monazite (Čopjaková et al., 2011).

The reason for the zoning observed in such low-T monazite is not clear. Considering the chemical and thermodynamic features, Milodowski and Zalasiewicz (1991) suggest REE speciation as organic and bicarbonate complexes during burial, with increasing stability of these complexes with increasing REE atomic number being responsible for zoning in the monazite nodules. However, solution complexation reactions involving organic, and/or the most common inorganic (carbonate, phosphate, hydroxide) ligands, leading to the general increase in solubility of REE from La to Lu in waters (Byrne and Lee, 1993; Lee and Byrne, 1992, 1993; Sonke and Salters, 2006; Wood, 1990), cannot fully explain the observed zoning pattern (core–rim increase in La and Ce together with a decrease in Nd + MREE). Instead, Burnotte et al. (1989) suggested that the zoning pattern could be explained by differences in the solubility of the individual REE phosphates. $REEPO_4$ solubility in aqueous solutions is poorly understood and there are conflicting results. Minimal solubility is observed for LREE between Ce and Sm; $LaPO_4$ solubility is substantially higher than neighbouring LREE, and for HREE solubility increases with increasing atomic number (Liu and Byrne, 1997). While Pourret et al. (2007) further discuss the ability of organic acids to preferentially complex MREE, Van Hoozen et al. (2020) use thermodynamic calculations to suggest the Nd-(MREE)/Ce/La compositional changes record a gradual temperature increase during subsequent growth. Lazareva et al. (2018) focusses on a hydrated REE-phosphate precursor to highlight the role of Eh–pH variations.

Hence, we suggest the precipitation of type 1 monazite cores (Nd- to Ce-dominant compositions) may have occured in thermally mature Middle Ordovician shales (late gas window, $\geq$210 °C), and under reducing conditions from slightly acidic to near neutral fluids that favoured MREE incorporation. Such conditions correspond to the diagenesis – anchizone transition. The REE source is driven by the competing influences of the refractory organic (MREE to HREE), Fe-oxyhydroxides (P, Ce and MREE) and siliciclastic fractions (L to HREE). Type 1 monazite rims evolving toward Ce compositions are assumed to result from ongoing REE fractionation in residual pore fluids and increasing temperatures in the anchizone facies. Such a formation process occurred around 405–400 Ma (403.6 ± 2.9 Ma), a period that corresponds to the anchizonal evolution of the shale of the Angers-Traveusot Formation. The REE zoning (low Th, U, Y – HREE) observed in authigenic NGM from the Angers-Traveusot Formation is described as typical of (very) low-grade metamorphic conditions (Alipour-Asll et al., 2012; Burnotte et al., 1989; Čopjaková et al., 2011; Donnot et al., 1973; Evans and Zalasiewicz, 1996; Evans et al., 2002; Halpin et al., 2014; Lev et al., 1998; Milodowski and Zalasiewicz, 1991; Rasmussen and Muhling, 2009). We therefore assume that NGM appearance is a phenomenon that occurs in response to increasing temperatures and is triggered at the diagenesis - anchizone transition after passing through the gas-generation window.

By contrast, type 2 and type 3 monazite-(Ce) grains may be anhedral or sub-euhedral and mostly micrometric in size, except when filling fractures. Type 2 monazite is distinctive in composition and its textural features indicate that it postdates type 1 monazite; type 2 monazite-(Ce) partially dissolves and replaces type 1 NGM (core and rim). Type 3 monazite shows mineral paragenesis and microtextures suggesting *syn*-metamorphic monazite formation linked to deformation of basin sediments similar to that described in Wilby et al. (2007). Both type 2 and type 3 monazite-(Ce) occurred late in the mineral paragenesis and are also assumed to have formed in the anchizone. Type 2 replacement monazite formed at ca. 390–375 Ma (382.6 ± 6.9 Ma) whereas type 3 vein filling was formed later at *ca.* 355–345 Ma (349.6 ± 6 Ma). Both monazite types may correspond to an open-system REE + Y redistribution during regional deformation stages.

When looking at the Pr distribution, the Pr versus Sm plot (Fig. 11c) highlights its singular behaviour during grain growth with respect to the positive and negative slope trends, also shown in Fig. 15. The fractionation of Pr or decoupling of Pr from Sm is difficult to explain here.. Based on the results described above, we suggest that the core of type 1 NGM crystallises at lower grade conditions than their rim overgrowths. For instance, cores may crystallise in the low-grade anchizone, whereas rims in the high-grade anchizone metamorphic conditions. If this assumption is true, then Pr could be an excellent temperature proxy for delineating low- to high-grade anchizone. Further studies could target its behaviour to evaluate the possible processes and conditions that lead to NGM nucleation.

In higher grade conditions, monazite grains evolve toward low Pr_{UCC} content and the highest $Log(La/Sm)_{UCC}$ ratios corresponding to metamorphic and magmatic monazites (Fig. 15a and b). Type 2 replacement monazite with the highest $Log(La/Sm)_{UCC}$ ratio and La_{UCC} values (Fig. 15b), corresponds to higher metamorphic grades, thus raising the question as to whether the temperature may have been raised locally (*e.g.* fluid circulation along faults and fractures).

5.4. Linking nodular grey monazite formation to geodynamic setting?

During the Cambro-Ordovician, the Armorican Massif was located along the northern margin of the Gondwana continent, in the Cadomian domain. This domain was composed of several terranes (*e.g.* Armorica, Avalonia) that drifted northward at the expense of the Iapetus Ocean in response to general slab roll-back dynamics (*e.g.* Nance et al., 2012). Many rifts developed, some of which aborted while others led to oceans opening up such as the Rheic Ocean which separated Avalonia from Armorica and the Medio-European Ocean (aka South Armorican – Massif Central Ocean) which developed between the North/Central Armorican domain (Armorica) and the South Armorican domain (Gondwana, Díez Montes et al., 2010; Nance et al., 2012; Vanderhaeghe et al., 2020). The rocks of interest in this study lie in the Central Armorican domain, where from the Cambrian to Lower Ordovician, *syn*-rift sequences combine suites of magmatic rocks with the deposition of

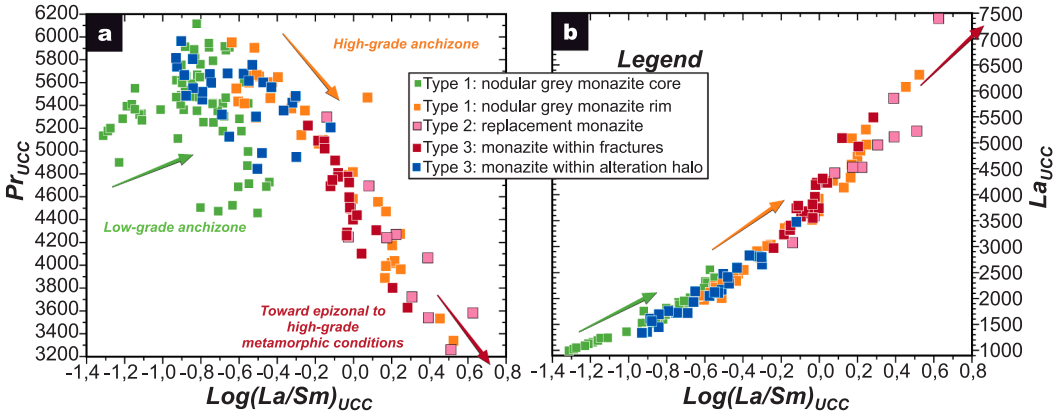

Fig. 15. a) PrUCC vs Log(La/Sm)UCC and b) LaUCC vs Log(La/Sm)UCC for the different generations of monazite showing REE fractionation during grain growth and overgrowths. Green and orange arrows suggest the compositional evolution for low-grade to high-grade anchizone metamorphic conditions respectively. The red arrow which may extend beyond the graph's limits, represents the compositional trend of high-grade anchizone to higher metamorphic conditions. UCC values are from McLennan (2001).

the "Initial Red Beds" (Pont-Réan Formation), then the Grès Armoricain Formation (Armorican sandstone, Fig. 16a). The post-rift sequences probably began with the deposition of the silty-clay intercalations of the upper part of the Grès Armoricain Formation and continued during the Middle Ordovician with the Angers-Traveusot Formation that was emplaced in an outer shelf environment dominated by black shale deposits (Ballèvre et al., 2012, Fig. 16b). In such an environment, the seawater REE-pattern reflects a combination of both intra-oceanic and fluvial processes (Pourret and Tuduri, 2017). During the transfer of stream water to the oceans, 90% of REE are removed from the solution by flocculation of colloidal materials that become trapped and sedimented onto the sea-floor (Fig. 16b'). Pourret and Tuduri (2017) thus consider continental shelves to be fertile sources of REE, and shelf sediments are compared to some metalliferous deep sea sediments (Kato et al., 2011).

The NGM precipitation began ca. 55 My after the deposition of the whole Angers-Traveusot sedimentary sequence, during the Lower Devonian (Emsian), and *ca.* 80 My after a marked increase in mantle

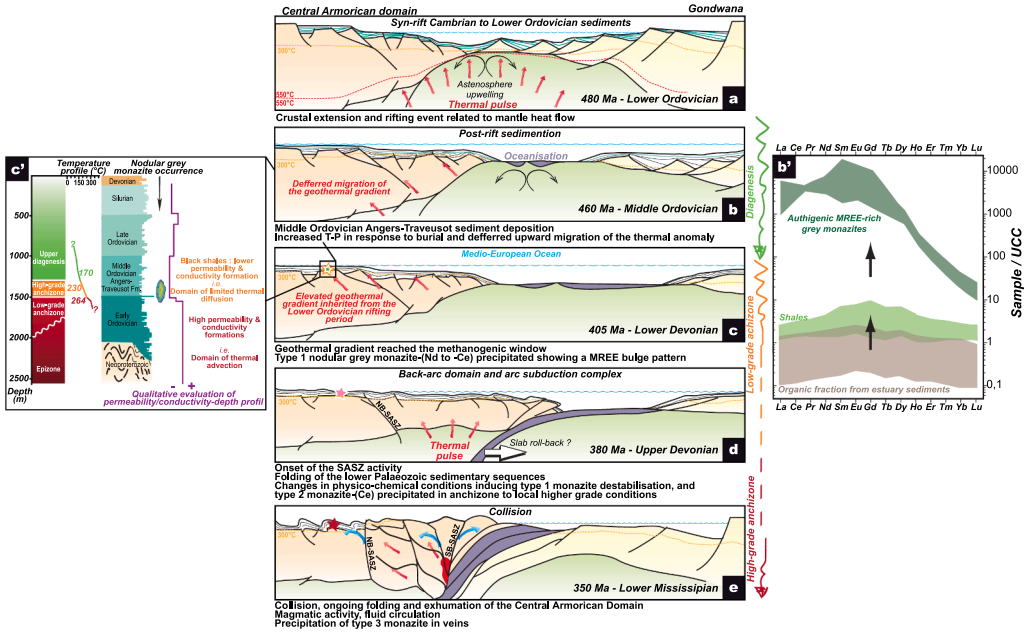

Fig. 16. Conceptual model of the plate-scale geodynamic setting between the Armorica and Gondwana margins showing the timing of formation of nodular grey monazite in the Central Armorican Domain (after Ballèvre et al., 2013;Paquette et al., 2017 and Tartese et al., 2015). a) Lower Ordovician and since the Cambrian: the margin of Gondwana is marked by an active period of extension in response to a thermal pulse, leading to the formation of a hyperextended domain and the formation of Armorica. b) Middle Ordovician: rift system evolves leading to the opening of the Medio-European Ocean. The post-rift Middle Ordovician black shales (Angers-Traveusot Formation) are deposited, whereas heat flow inherited from the rifting stage migrates upward in the crust. (b') From the Ordovician to Devonian, the diagenesis – lower-anchizone boundary migrated upward in the Angers-Traveusot Formation brought about by the heat flux and favouring both the progressive evolution of sea muds into black-shales and the precipitation of MREE-rich type 1 monazite. REE diagram after Pourret and Tuduri (2017). c) Early Devonian: the Medio-European Ocean reaches its maximum width. Pre-orogenic sediments are deposited while the surface temperature gradient inherited from the rifting stage still increases and reaches 300 °C in the Lower Ordovician sandstones (Grés Armoricain Formation). (c')The high-permeability and conductivity of that formation favours heat advection whereas black shales with lower permeability and conductivity underwent a limited thermal diffusion and enter the methanogenic window. d) Late Devonian: the Medio-European Ocean is starting to subduct beneath Armorica. This period is related to the early stages of the Variscan belt such as the onset of the South Armorican Shear Zone activity and folding of the lower Palaeaozoic formations. Note the high heat flux may be persistent in the Central Armorican Domain due to the subduction zone and may have led to destabilisation of nodular monazite grains into type 2 metamorphic monazite. e) Early Mississippian: collision between Armorica and Gondwana occurs. The Variscan orogenic front evolves inducing ongoing heat flow and fluid circulation (blue arrows) in the Central Armorican Domain and development of type 3 metamorphic monazite. NB-SASZ: North Branch of the South Armorican Shear Zone; SB-SASZ: South Branch of the South Armorican Shear Zone.

heat flow that initiated rifting. Indeed, we suggest that the NGM formation was linked to late evolution of the basin infilling prior to the Variscan collision and was especially dependent on the thermal evolution of the upper crust, with REE remobilisation developing in response to regional deformation and fluid circulation (forming type-2 replacement or type-3 monazite in late fractures).

In our model (Fig. 16), the Cambro-Ordovician rifting accommodated by a marked asthenospheric upwelling inducing a large heat flux at the base of the crust, controlled the thermal evolution of the Ordovician to Devonian sediments, the OM maturation, and MREE, P and water release. Indeed, our observations indicate that in the Grand-Fougeray area, the Angers-Traveusot Formation reached its maximum temperature at the end of the post-rift period, *ca.* 80 My after the onset of the rifting: a period and related processes that created an environment conducive to NGM precipitation at the boundary between high-grade diagenetic to low-grade anchizone conditions. Numerical simulations have already described such temperature peaks, strongly post-dating the *syn*-rift sedimentary infill and close to the surface (*e.g.* Saspiturry et al., 2020). In fact, these authors explain that at the time of rifting, the increase in mantle heat flow only warms the lower part of the crust, while the coexisting sedimentation does not experience this effect. These sediments are heated later in response to the progressive but slow migration of the advective heat flow through the crust, *i.e.* between 60 and 100 My after the initial thermal pulse. Our palaeo-temperature estimations from KI values make it possible to evaluate the geothermal gradient in the basin prior to the Variscan orogeny (Fig. 16c') in the Grand Fougeray area. The Angers-Traveusot Formation is assumed to have been buried at shallow depth to a minimum of 1.5 km excluding the seawater column. Based on the palaeo-temperature estimations, an abnormally high geothermal gradient would be required (*ca.* 100 °C/km in a lithostatic regime). For instance, Saspiturry et al. (2020) propose a temperature gradient not exceeding 60 °C/km in their model. This raises questions as to the incomplete nature of the Devonian sedimentary sequences and suggests possible décollements in these formations as previously suggested by Ballèvre et al, (2013). The whole Ordovician to Devonian sedimentary sequence might have been thicker than previously supposed. Hence, we assume that around 410–400 Ma, the high-permeability and conductivity of both the deformed Neoproterozoic formations and the Lower Ordovician sandstone favoured heat advection rather than diffusion; whereas the shales from the Angers-Traveusot and the upper part of the Grès Armoricain formations were of lower permeability and conductivity which limited the thermal diffusion, thus explaining the large temperature range between the bottom and the top of the sedimentary sequence (Fig. 5a).

The U/Pb dates (Fig. 14) recorded by the different monazite generations also reveal a long-lasting process of crystallisation, dissolution and recrystallisation that initiated during the early Devonian and continued up to the onset of the Carboniferous. Around 380 Ma (Fig. 16d), the closure of the Medio-European Ocean is explained by its northward subduction and the progressive accretion of small allochthonous terranes (oceanic units and outer margins of Gondwana) leading to the earliest phase of folding in the Central Armorican Domain of interest here. Such a setting may be consistent with long term heat flow above the continental subduction panel, probably maintained by the subduction zone and possible slab roll-back. Type 2 replacement monazite developed *ca.* 385–375 My ago around the transition from the middle to late Devonian (Givetian / Frasnian), a period that corresponds to the early Variscan deformation stage (folding, cleavage, faulting) which probably increased rock permeability and favoured fluid circulation and veining in the lower part of the Middle Ordovician Angers-Traveusot Formation as well as oxidation of the OM. Fluid circulation from mixed sources may also explain the replacement process. The metamorphic conditions also correspond to the anchizone domain, although some very high $Log(La/Sm)_{UCC}$ and low Pr_{UCC} may suggest that epizone conditions prevailed locally. Note that Tuduri et al. (2014) provided a U/Pb ID-TIMS age of 384 ± 1.6 Ma for a postulated type 1 nodular monazite grain from La Monnerie concentrate. We reinterpret this finding in this study and heavy grains are now considered to be type 2 monazite replacements.

Later stages correspond to the main exhumation of the subducted Gondwana crust, nappe stacking south of the Central Armorican Domain at ca. 360–350 Ma (Fig. 16e) and possibly the partial exhumation of the Angers-Traveusot Formation due to folding. Overall, the Central Armorican Domain remained unscathed by major Variscan deformation during this period, but this does not exclude the possibility of high heat flow, fluid circulation and monazite deposition (Gloaguen et al., 2007; Pochon et al., 2018; Tartèse et al., 2015). Consequently, late type 3 monazite is related to veining *ca.* 350 My ago during the Mississipian (Tournaisian).

NGM also formed in the central Welsh Basin during the early Devonian (417 ± 11 Ma U/Pb isotope dilution / 419 ± 14 Ma, SHRIMP Th/Pb age, Evans & Zalasiewicz, 1996; Evans et al., 2002 respectively). This age has also been interpreted as being related to diagenetic processes and compactional dewatering associated with the rocks passing though the smectite–illite transition during HC expulsion. This period coincides with an early phase of convergence in the southern part of Avalonia, characterised by northward subduction, the maintenance of an inherited thermal anomaly, linked to the opening of the Rheic Ocean 80 My earlier (Nance et al., 2012; Vanderhaeghe et al., 2020).

6. Concluding remarks

In the Grand-Fougeray area, the Middle Ordovician Angers-Traveusot Formation reached peak metamorphism in the low-grade anchizone facies prior to the Variscan folding event. Nodular grey monazite formed during the early Devonian ca. 405 to 400 Ma. It can be divided into -Nd and -Ce endmembers with marked MREE-enrichment. It formed in response to processes initiated during diagenenesis and continued to low-grade anchizone metamorphic conditions by a series of diagenetic processes controlled by different competing influences such as OM maturation, Fe oxide/hydroxide reduction, clay transformation, and fluid migration. Grains are assumed to be stable in the anchizone metamorphic conditions from *ca.* 215 °C to 300 °C and destabilized in the epizone domain. Later stages of monazite formation are related to compressional deformation that occurred from 385 to 350 Ma and consisted of monazite-Ce precipitation in the anchimetamorphic domain as well. Therefore the geodynamic setting had a strong influence on nodular grey monazite crystallisation as it catalysed the thermal maturation of both sediments and OM in response to the inheritance of an 80 My old elevated mantle heat flow, which led to the opening of the Medio-European Ocean. Such a thermal input might also need to be considered in other settings where nodular grey monazite occurs at the onset of mountain building or in the distal thermal aureoles of magmatic intrusions (Alipour-Asll et al., 2012; Lazareva et al., 2018; Rosenblum and Mosier, 1983; Wing et al., 2003).

Consequently, palaeocontinental shelves may be considered as traps for potential REE + Y sources (Fig. 16a) and interesting sites for exploration as suggested by Pourret and Tuduri (2017). Although authigenic nodular grey monazite occurrences are not currently economically viable, heavy nodules may constitute an interesting by-product for the mineral sand industry as REE + Y are increasingly used in a wide range of low-carbon energy production processes and high-technology devices. Often, the general association of common monazite-Ce with radioactive elements such as Th and sometimes U, constitutes a major barrier to project development, which is not the case for these nodular grey monazite occurrences.

Many occurrences of nodular grey monazite are known in the Americas, Asia, Europe and Africa (Rosenblum and Mosier, 1983; Charles et al., 2022) and future studies may show that they are controlled by a high heat flux that could be linked to a specific geodynamic setting or to local heat flow sources such as thermal haloes around magmatic intrusions.

To aid conceptual targeting, nodular grey monazite prospectivity models might focus on understanding the thermal evolution of sedimentary basins. For instance, our model explores the geothermal regime, *i.e.* an elevated mantle heat flow, which controls the tectonic architecture at the crustal scale during basin development. A similar approach can be applied when considering the thermal evolution of sedimentary sequences in response to magmatic intrusions and contact aureole development. We suggest that fertile schists must reach the anchizone domain to trigger the precipitation of nodular grey monazite, but we also expect that epizonal metamorphic conditions may destabilise this monazite. In such a context, nodular grey monazite is preserved by protecting the mineralised shales from subsequent tectonothermal processes such as deep burial and increasing regional and/or contact metamorphism. This nodular grey monazite with MREE-rich patterns thus constitutes an interesting alternative source of REE because of its very low content in both Th and U and negligible radiological impact if mined (Donnot et al., 1973; García-Tenorio et al., 2018; Rosenblum and Mosier, 1983; Tuduri et al., 2015). At present, however the placers are of limited economical interest.

Declaration of Competing Interest

The authors declare that they have no known competing financial interests or personal relationships that could have appeared to influence the work reported in this paper.

Data availability

Data will be made available on request.

Acknowledgements

The work was developed within both the ASTER and TRACT projects, supported by the French National Research Agency; ANR (project ANR-11-ECOT-002) and the BRGM respectively. Many thanks to Kensaï Artis, Alexandre Borniche, Faddy Nassif, Pierre-Marie Bastien, Léo Thévenin, Baptiste Vincens and Sébastien Potel for their contributions to the XRD analysis, to Mohammed Boussafir for his precious comments on Rock-EVAL interpretation, Abdeltif Lahfid for Raman, Denis Gapais and Yannick Branquet for discussions on the ages and the palaeogeodynamics, and Frances for edits. We thank reviewers for their constructive comments.

Appendix A. Supplementary data

Supplementary data to this article can be found online at https://doi.org/10.1016/j.oregeorev.2023.105583.

References

Alipour-Asll, M., Mirnejad, H., Milodowski, A.E., 2012. Occurrence and paragenesis of diagenetic monazite in the upper Triassic black shales of the Marvast region, South Yazd, Iran. Mineral. Petrol. 104, 197–210.
Ballèvre, M., Bosse, V., Ducassou, C., Pitra, P., 2009. Palaeozoic history of the Armorican Massif: Models for the tectonic evolution of the suture zones. C. R. Geosci. 341, 174–201.
Ballèvre, M., Fourcade, S., Capdevila, R., Peucat, J.J., Cocherie, A., Fanning, C.M., 2012. Geochronology and geochemistry of Ordovician felsic volcanism in the Southern Armorican Massif (Variscan belt, France): Implications for the breakup of Gondwana. Gondw. Res. 21, 1019–1036.
Ballèvre, M., Bosse, V., Dabard, M.-P., Ducassou, C., Fourcade, S., Paquette, J.-L., Peucat, J.-J., Pitra, P., 2013. Histoire Géologique du massif Armoricain: Actualité de la recherche. Bull. Soc. Géol. Minéral. Bretagne (D) 10–11, 5–96.
Bau, M., 1996. Controls on the fractionation of isovalent trace elements in magmatic and aqueous systems: evidence from Y/Ho, Zr/Hf, and lanthanide tetrad effect. Contrib. Miner. Petrol. 123, 323–333.
Bea, F., 1996. Residence of REE, Y, Th and U in granites and crustal protoliths; Implications for the chemistry of crustal melts. J. Petrol. 37, 521–552.
Brun, J.P., Guennoc, P., Truffert, C., Vairon, J., 2001. Cadomian tectonics in northern Brittany: a contribution of 3-D crustal-scale modelling. Tectonophysics 331, 229–246.
Burnotte, E., Pirard, E., Michel, G., 1989. Genesis of gray monazites; evidence from the Paleozoic of Belgium. Econ. Geol. 84, 1417–1429.
Byrne, R.H., Lee, J.H., 1993. Comparative yttrium and rare earth element chemistries in seawater. Mar. Chem. 44, 121–130.
Calcagno, P., Chilès, J.P., Courrioux, G., Guillen, A., 2008. Geological modelling from field data and geological knowledge: Part I. Modelling method coupling 3D potential-field interpolation and geological rules. Phys. Earth Planet. In. 171, 147–157.
Chantraine, J., Autran, A., Cavelier, C., Clozier, L., 2003. Carte géologique de la France à l'échelle du millionième, 6e édition révisée ed. BRGM, Orléans, France.
Charles, N., Tuduri, J., Lefebvre, G., Pourret, O., Gaillard, F., Goodenough, K., 2022. Ressources en terres rares de l'Europe et du Groenland: potentiel minier et enjeux. In: Decrée, S. (Ed.), Ressources Métalliques: Cadre Géodynamique Et Exemples Remarquables En Europe. ISTE Editions Ltd, London, United Kingdom, pp. 1–137.
Choukroune, P., Lopez-Munoz, M., Ouali, J., 1983. Cisaillement ductile sud-armoricain et déformations discontinues associées: mise en évidence de la déformation régionale non coaxiale dextre. Comptes Rendus - Academie des Sciences, Serie II 296, 657–660.
Cobert, C., Baele, J.-M., Boulvais, P., Decrée, S., Dupont, N., Spagna, P., 2015. Grey monazite paleoplacers in Lower Cretaceous continental formations in the Mons Basin, Belgium, SGA2015: 13th Biennial meeting, pp. 1173-1176.
Cooper, D.C., Basham, I.R., Smith, T.K., 1983. On the occurrence of an unusual form of monazite in panned stream sediments in Wales. Geol. J. 18, 121–127.
Čopjaková, R., Novák, M., Franců, E., 2011. Formation of authigenic monazite-(Ce) to monazite-(Nd) from Upper Carboniferous graywackes of the Drahany Upland: Roles of the chemical composition of host rock and burial temperature. Lithos 127, 373–385.
Coppin, F., Berger, G., Bauer, A., Castet, S., Loubet, M., 2002. Sorption of lanthanides on smectite and kaolinite. Chem. Geol. 182, 57–68.
Dabard, M.-P., Loi, A., Paris, F., 2007. Relationship between phosphogenesis and sequence architecture: Sequence stratigraphy and biostratigraphy in the Middle Ordovician of the Armorican Massif (NW France). Palaeogeogr. Palaeoclimatol. Palaeoecol. 248, 339–356.
Dabard, M.-P., Loi, A., 2012. Environmental control on concretion-forming processes: Examples from Paleozoic terrigenous sediments of the North Gondwana margin, Armorican Massif (Middle Ordovician and Middle Devonian) and SW Sardinia (Late Ordovician). Sed. Geol. 267–268, 93–103.
Dabard, M.P., Loi, A., Paris, F., Ghienne, J.F., Pistis, M., Vidal, M., 2015. Sea-level curve for the Middle to early Late Ordovician in the Armorican Massif (western France): Icehouse third-order glacio-eustatic cycles. Palaeogeogr. Palaeoclimatol. Palaeoecol. 436, 96–111.
Dadet, P., Herrouin, Y., Laville, P., Paris, F., 1987. Carte géol. France (1/50000), feuille Bain-de-Bretagne (388). BRGM, Orléans, France.
Dadet, P., Herrouin, Y., Blanchet, C., Bardy, P., Colleau, A., 1995. Carte géol. France (1/50000), feuille Pipriac (387). BRGM, Orléans, France.
Díez Montes, A., Martínez Catalán, J.R., Bellido Mulas, F., 2010. Role of the Ollo de Sapo massive felsic volcanism of NW Iberia in the Early Ordovician dynamics of northern Gondwana. Gondw. Res. 17, 363–376.
Donnot, M., Guigues, J., Lulzac, Y., Magnien, A., Parfenoff, A., Picot, P., 1973. Un nouveau type de gisement d'europium: la monazite grise à europium en nodules dans les schistes paléozoïques de Bretagne. Miner. Deposita 8, 7–18.
Durand, J., Noblet, C., 1986. Paléocourants dans la Formation du Grès armoricain: persistance des mécanismes de transport en domaine cratonique. Rev. Géol. Dyn. Géogr. Phys. 27, 13–26.
Engi, M., 2017. Petrochronology based on REE-minerals: monazite, allanite, xenotime, apatite. Rev. Mineral. Geochem. 83, 365–418.
Evans, J., Zalasiewicz, J., 1996. U-Pb, Pb-Pb and Sm-Nd dating of authigenic monazite: implications for the diagenetic evolution of the Welsh Basin. Earth Planet. Sci. Lett. 144, 421–433.
Evans, J.A., Zalasiewicz, J.A., Fletcher, I., Rasmussen, B., Pearce, N.J.G., 2002. Dating diagenetic monazite in mudrocks: constraining the oil window? J. Geol. Soc. 159, 619.
Ferreiro Mählmann, R., 2001. Correlation of very low grade data to calibrate a thermal maturity model in a nappe tectonic setting, a case study from the Alps. Tectonophysics 334, 1–33.
Freslon, N., Bayon, G., Toucanne, S., Bermell, S., Bollinger, C., Chéron, S., Etoubleau, J., Germain, Y., Khripounoff, A., Ponzevera, E., Rouget, M.-L., 2014. Rare earth elements and neodymium isotopes in sedimentary organic matter. Geochim. Cosmochim. Acta 140, 177-198.
Frey, M., 1987. Low Temperature Metamorphism, in: Frey, M. (Ed.), Frey, M. (ed.) (1987), Glasgow and London, 351 pp. Frey, M., Desmons, J. and Neubauer, F. (eds.) ed. Blackie & Son Limited, Glasgow, London, p. 351.
Gapais, D., Le Corre, C., 1980. Is the Hercynien belt of Brittany a major shear zone? Nature 288, 574–576.
Gapais, D., Brun, J.-P., Gumiaux, C., Cagnard, F., Ruffet, G., Le Carlier De Veslud, C., 2015. Extensional tectonics in the Hercynian Armorican belt (France). An overview. Bull. Soc. Geol. Fr. 186, 117–129.
García-Tenorio, R., Manjón, G., Vioque, I., Jiménez-Ramos, M.C., Mantero, J., Díaz-Francés, I., 2018. Grey monazite (rare earths) mining in centre of Spain: Characterization and pre-operational radiological evaluation. Chemosphere 208, 691–697.
Gensel, P.G., 2008. The Earliest Land Plants. Annual Review of Ecology, Evolution, and Systematics 39, 459-477.
Gloaguen, E., Branquet, Y., Boulvais, P., Moëlo, Y., Chauvel, J.-J., Chiappero, P.-J., Marcoux, E., 2007. Palaeozoic oolitic ironstone of the French Armorican Massif: a

chemical and structural trap for orogenic base metal–As–Sb–Au mineralisation during Hercynian strike-slip deformation. Miner. Deposita 42, 399–422.
Guigues, J., Devismes, P., 1969. La prospection minière à la batée dans le Massif Armoricain: méthodes, résultats, atlas minéralogique. Mémoires du BRGM 71, 167.
Guigues, J., Sapinart, J., 1967. Monazite à europium armoricaine. Résumé des travaux effectués et état des connaissances au 28.2.1967. BRGM 40.
Guillocheau, F., Rolet, J., 1982. La sedimentation paleozoique ouest-armoricaine; histoire sedimentaire; relations tectonique-sedimentation. Bull. Soc. Géol. Minéral. Bretagne 14, 45–62.
Gumiaux, C., Gapais, D., Brun, J.P., Chantraine, J., Ruffet, G., 2004. Tectonic history of the Hercynian Armorican Shear belt (Brittany, France). Geodin. Acta 17, 289–307.
Guyonnet, D., Planchon, M., Rollat, A., Tuduri, J., 2016. Dynamic representation of flows and stocks of metals in the Economy. In: Chagnes, A., Cote, G., Ekberg, C., Nilsson, M., Retegan, T. (Eds.), WEEE Recycling: Research, Development, and Policies. Elsevier, pp. 31–52.
Haley, B.A., Klinkhammer, G.P., McManus, J., 2004. Rare earth elements in pore waters of marine sediments. Geochim. Cosmochim. Acta 68, 1265–1279.
Halpin, J.A., Jensen, T., McGoldrick, P., Meffre, S., Berry, R.F., Everard, J.L., Calver, C. R., Thompson, J., Goemann, K., Whittaker, J.M., 2014. Authigenic monazite and detrital zircon dating from the Proterozoic Rocky Cape Group, Tasmania: Links to the Belt-Purcell Supergroup, North America. . Precambrian Res. 250, 50–67.
Henderson, P., 1984. Rare earth element geochemistry. Elsevier, Amsterdam, NL.
Henry, J.-L., 1989. Paléoenvironnements et dynamique de faunes de Trilobites dans l'Ordovicien (Llanvirn Supérieur-caradoc basal) du Massif Armoricain (France). Palaeogeogr. Palaeoclimatol. Palaeoecol. 73, 139–153.
Herron, M.M., 1988. Geochemical classification of terrigenous sands and shales from core or log data. J. Sediment. Res. 58, 820–829.
Janots, E., Engi, M., Berger, A., Allaz, J., Schwarz, J.O., Spandler, C., 2008. Prograde metamorphic sequence of REE minerals in pelitic rocks of the Central Alps: implications for allanite–monazite–xenotime phase relations from 250 to 610°C. J. Metam. Geol. 26, 509–526.
Janots, E., Berger, A., Engi, M., 2011. Physico-chemical control on the REE minerals in chloritoid-grade metasediments from a single outcrop (Central Alps, Switzerland). Lithos 121, 1–11.
Jarvis, I., 1994. Phosphorite geochemistry: state-of-the-art and environmental concerns. Eclogae Geol. Helv. 87, 643–700.
Jégouzo, P., 1980. The South Armorican Shear Zone. J. Struct. Geol. 2, 39–47.
Johannesson, K.H., Zhou, X., 1999. Origin of middle rare earth element enrichments in acid waters of a Canadian High Arctic lake. Geochim. Cosmochim. Acta 63, 153–165.
Johannesson, K.H., Stetzenbach, K.J., Hodge, V.F., 1997. Rare earth elements as geochemical tracers of regional groundwater mixing. Geochim. Cosmochim. Acta 61, 3605–3618.
Jones, A.P., Wall, F., Williams, C.T., 1996. Rare earth minerals. Chemistry, origin and ore deposits. Chapman & Hall, London, UK.
Kato, Y., Fujinaga, K., Nakamura, K., Takaya, Y., Kitamura, K., Ohta, J., Toda, R., Nakashima, T., Iwamori, H., 2011. Deep-sea mud in the Pacific Ocean as a potential resource for rare-earth elements. Nat. Geosci. 4, 535–539.
Kim, J.-H., Torres, M.E., Haley, B.A., Kastner, M., Pohlman, J.W., Riedel, M., Lee, Y.-J., 2012. The effect of diagenesis and fluid migration on rare earth element distribution in pore fluids of the northern Cascadia accretionary margin. Chem. Geol. 291, 152–165.
Knoper, M., Armstrong, R., Andreoli, M., Ashwal, L., 2000. The Steenkampskraal monazite vein: a subhorizontal stretching shear zone indicating extensional collapse of Namaqualand at 1033 Ma? J. Afr. Earth Sc. 31, 38–39.
Lafargue, E., Marquis, F., Pillot, D., 1998. Rock-Eval 6 Applications in Hydrocarbon Exploration, Production, and Soil Contamination Studies. Rev. Inst. Fr. Pét. 53, 421–437.
Lazareva, E.V., Zhmodik, S.M., Prokopiev, A.V., Karmanov, N.S., Sergeenko, A.I., 2018. Nodular monazite from placers in the Kular Ridge (Arctic Siberia, Russia): Composition and age. Russ. Geol. Geophys. 59, 1330–1347.
Le Corre, C., 1975. Analyse comparée de la cristallinité des micas dans le Briovérien et le Paléozoique centre-armoricains; zonéographie et structure d'un domaine épizonal. Bull. Soc. Geol. Fr. S7-XVII, 547–553.
Le Corre, C., Auvray, B., Ballèvre, M., Robardet, M., 1991. Le massif armoricain. Sci. Géol. Bull. 44, 31–103.
Le Corre, C., Le Theoff, B., 1976. Zoneographie de la deformation finie, de la fabrique et du metamorphisme dans un segment de la chaine hercynienne armoricaine. Bull. Soc. Geol. Fr. S7-XVIII, 1435–1442.
Lee, J.H., Byrne, R.H., 1992. Examination of comparative rare earth element complexation behavior using linear free-energy relationships. Geochim. Cosmochim. Acta 56, 1127–1137.
Lee, J.H., Byrne, R.H., 1993. Complexation of trivalent rare earth elements (Ce, Eu, Gd, Tb, Yb) by carbonate ions. Geochim. Cosmochim. Acta 57, 295–302.
Lee, J., Bazilian, M., Sovacool, B., Hund, K., Jowitt, S.M., Nguyen, T.P., Månberger, A., Kah, M., Greene, S., Galeazzi, C., Awuah-Offei, K., Moats, M., Tilton, J., Kukoda, S., 2020. Reviewing the material and metal security of low-carbon energy transitions. Renewable Sustainable Energy Rev. 124, 109789.
Lev, S.M., McLennan, S.M., Meyers, W.J., Hanson, G.N., 1998. A petrographic approach for evaluating trace-element mobility in a black shale. J. Sediment. Res. 68, 970–980.
Lipin, B.R., McKay, G.A., 1989. Geochemistry and mineralogy of rare earth elements. Mineralogical Society of America, Washington, DC, US.
Liu, X., Byrne, R.H., 1997. Rare earth and yttrium phosphate solubilities in aqueous solution. Geochim. Cosmochim. Acta 61, 1625–1633.
Lulzac, Y., 1969. Contribution à la recherche et à l'étude des gîtes primaires de monazite grise à europium dans le massif armoricain. BRGM, DRMM 69 (06), 41.
März, C., Poulton, S.W., Beckmann, B., Küster, K., Wagner, T., Kasten, S., 2008. Redox sensitivity of P cycling during marine black shale formation: Dynamics of sulfidic and anoxic, non-sulfidic bottom waters. Geochim. Cosmochim. Acta 72, 3703–3717.
Matys Grygar, T., Mach, K., Martinez, M., 2019. Checklist for the use of potassium concentrations in siliciclastic sediments as paleoenvironmental archives. Sed. Geol. 382, 75–84.
McLennan, S.M., 1989. Rare earth elements in sedimentary rocks; influence of provenance and sedimentary processes. Rev. Mineral. Geochem. 21 (1), 169–200.
McLennan, S.M., 2001. Relationships between the trace element composition of sedimentary rocks and upper continental crust. Geochem. Geophys. Geosyst. 2, 1021.
Merriman, R.J., Frey, M., 1999. Patterns of very low-grade metamorphism in metapelitic rocks. In: Frey, M., Robinson, D. (Eds.), Low-Grade Metamorphism. Blackwell Science, Oxford, pp. 61–107.
Michard, A., 1989. Rare earth element systematics in hydrothermal fluids. Geochim. Cosmochim. Acta 53, 745–750.
Milodowski, A.E., Zalasiewicz, J.A., 1991. Redistribution of rare earth elements during diagenesis of turbidite/hemipelagite mudrock sequences of Llandovery age from central Wales. Geol. Soc. London Spec. Publ. 57, 101.
Moëlo, Y., Rouer, O., Bouhnik-Le Coz, M., 2008. From diagenesis to hydrothermal recrystallization: polygenic Sr-rich fluorapatite from the oolitic ironstone of Saint-Aubin-des-Châteaux (Armorican Massif, France). Eur. J. Mineral. 20, 205–216.
Montel, J.-M., Foret, S., Veschambre, M., Nicollet, C., Provost, A., 1996. Electron microprobe dating of monazite. Chem. Geol. 131, 37–53.
Nance, R.D., Gutiérrez-Alonso, G., Keppie, J.D., Linnemann, U., Murphy, J.B., Quesada, C., Strachan, R.A., Woodcock, N.H., 2012. A brief history of the Rheic Ocean. Geosci. Front. 3, 125-135.
Noack, C.W., Dzombak, D.A., Karamalidis, A.K., 2014. Rare earth element distributions and trends in natural waters with a focus on groundwater. Environ. Sci. Tech. 48, 4317–4326.
Paquette, J.L., Ballèvre, M., Peucat, J.J., Cornen, G., 2017. From opening to subduction of an oceanic domain constrained by LA-ICP-MS U-Pb zircon dating (Variscan belt, Southern Armorican Massif, France). Lithos 294–295, 418–437.
Parrish, R.R., 1990. U-Pb dating of monazite and its application to geological problems. Can. J. Earth Sci. 27, 1431–1450.
Pepper, A.S., Corvi, P.J., 1995. Simple kinetic models of petroleum formation. Part I: oil and gas generation from kerogen. Mar. Pet. Geol. 12, 291–319.
Pochon, A., Gloaguen, E., Branquet, Y., Poujol, M., Ruffet, G., Boiron, M.-C., Boulvais, P., Gumiaux, C., Cagnard, F., Gouazou, F., Gapais, D., 2018. Variscan Sb-Au mineralization in Central Brittany (France): A new metallogenic model derived from the Le Semnon district. Ore Geol. Rev. 97, 109–142.
Poitrasson, F., Chenery, S., Bland, D.J., 1996. Contrasted monazite hydrothermal alteration mechanisms and their geochemical implications. Earth Planet. Sci. Lett. 145, 79–96.
Potel, S., Mählmann, R.F., Stern, W.B., Mullis, J., Frey, M., 2006. Very low-grade metamorphic evolution of pelitic rocks under high-pressure/low-temperature conditions, NW New Caledonia (SW Pacific). J. Petrol. 47, 991–1015.
Pourret, O., Davranche, M., Gruau, G., Dia, A., 2007. Rare earth elements complexation with humic acid. Chem. Geol. 243, 128–141.
Pourret, O., Tuduri, J., 2017. Continental shelves as potential resource of rare earth elements. Sci. Rep. 7, 5857.
Rasmussen, B., Muhling, J.R., 2007. Monazite begets monazite: evidence for dissolution of detrital monazite and reprecipitation of syntectonic monazite during low-grade regional metamorphism. Contrib. Miner. Petrol. 154, 675–689.
Rasmussen, B., Buick, R., Taylor, W.R., 1998. Removal of oceanic REE by authigenic precipitation of phosphatic minerals. Earth Planet. Sci. Lett. 164, 135–149.
Rasmussen, B., Muhling, J.R., 2009. Reactions destroying detrital monazite in greenschist-facies sandstones from the Witwatersrand basin, South Africa. Chem. Geol. 264, 311–327.
Read, D., Cooper, D.C., McArthur, J.M., 1987. The composition and distribution of nodular monazite in the lower Palaeozoic rocks of Great Britain. Mineral. Mag. 51, 271–280.
Read, D., Andreoli, M.A.G., Knoper, M., Williams, C.T., Jarvis, N., 2002. The degradation of monazite: Implications for the mobility of rare-earth and actinide elements during low-temperature alteration. Eur. J. Mineral. 14, 487–498.
Rillard, J., Pourret, O., Censi, P., Inguaggiato, C., Zuddas, P., Toulhoat, P., Gombert, P., Brusca, L., 2019. Behavior of rare earth elements in an aquifer perturbed by CO2 injection: Environmental implications. Sci. Total Environ. 687, 978–990.
Robardet, M., Doré, F., 1988. The late Ordovician diamictic formations from southwestern Europe: North-Gondwana glaciomarine deposits. Palaeogeogr. Palaeoclimatol. Palaeoecol. 66, 19–31.
Robardet, M., Verniers, J., Feist, R., Paris, F., 1994. Le Paléozoïque anté-varisque de France, contexte paléogéographique et géodynamique. Géol. Fr. 3, 3–31.
Rosenblum, S., Mosier, E.L., 1983. Mineralogy and occurrence of europium-rich dark monazite. U.S. Geol. Surv. Prof. Pap. 1181, 67.
Salgueiro, R., Inverno, C., de Oliveira, D.P.S., Guimarães, F., Lencastre, J., Rosa, D., 2020. Alluvial nodular monazite in Monfortinho (Idanha-a-Nova, Portugal): Regional distribution and genesis. J. Geochem. Explor. 210.
Saspiturry, N., Lahfid, A., Baudin, T., Guillou-Frottier, L., Razin, P., Issautier, B., Le Bayon, B., Serrano, O., Lagabrielle, Y., Corre, B., 2020. Paleogeothermal gradients across an inverted hyperextended rift system: example of the Mauléon fossil rift (Western Pyrenees). Tectonics 39, e2020TC006206.
Schulz, B., Brätz, H., Bombach, K., Krenn, E., 2007. In-situ Th-Pb dating of monazite by 266 nm laser ablation and ICP-MS with a single collector, and its control by EMP analysis. Z. Angew. Geol. 35, 377–392.

Seydoux-Guillaume, A.-M., Montel, J.-M., Bingen, B., Bosse, V., de Parseval, P., Paquette, J.-L., Janots, E., Wirth, R., 2012. Low-temperature alteration of monazite: Fluid mediated coupled dissolution–precipitation, irradiation damage, and disturbance of the U-Pb and Th–Pb chronometers. Chem. Geol. 330–331, 140–158.
Sonke, J.E., Salters, V.J.M., 2006. Lanthanide–humic substances complexation. I. Experimental evidence for a lanthanide contraction effect. Geochim. Cosmochim. Acta 70, 1495–1506.
Spear, F.S., Pyle, J.M., 2002. Apatite, Monazite, and Xenotime in Metamorphic Rocks. Rev. Mineral. Geochem. 48, 293–335.
Suire, P., Dabard, M.-P., Chauvel, J.-J., 1991. The Ordovician Red Beds of Brehec (Armorican Massif): a sedimentological study. Comptes Rendus - Academie des Sciences, Serie II 312, 721–727.
Tartèse, R., Poujol, M., Gloaguen, E., Boulvais, P., Drost, K., Košler, J., Ntaflos, T., 2015. Hydrothermal activity during tectonic building of the Variscan orogen recorded by U-Pb systematics of xenotime in the Grès Armoricain formation, Massif Armoricain. France. Mineral. Petrol. 109, 485–500.
Tera, F., Wasserburg, G.J., 1972. U-Th-Pb systematics in three Apollo 14 basalts and the problem of initial Pb in lunar rocks. Earth Planet. Sci. Lett. 14, 281–304.
Tomascak, P.B., Krogstad, E.J., Walker, R.J., 1996. U-Pb monazite geochronology of granitic rocks from Maine: implications for late Paleozoic tectonics in the Northern Appalachians. J. Geol. 104, 185–195.
Trautmann, F., Donnot, M., Lemaire, D., Cagnet-Mawhin, M.P., 1987. Carte géol. France (1/50000), Feuille Nozay (420). BRGM, Orléans, France.
Trautmann, F., Delfour, J., Fourniguet, J., Scanvic, J.Y., Dubreuil, G., Pivette, B., Prian, J. P., Militon, C., Manigault, B., 1984. Carte géol. France (1/50000), feuille Redon (420). BRGM, Orléans, France.
Tuduri, J., Pourret, O., Gloaguen, E., Gouin, J., Potel, S., Dörr, W., Colin, S., Chevillard, M., 2014. U-Pb age and geochemistry of authigenic monazites of the Armorican Massif. Implications for formation of monazite-(MREE) from paleozoic shales, 24ème Réunion des Sciences de la Terre, Pau, France, pp. 342-343.
Tuduri, J., Charles, N., Guyonnet, G., Melleton, J., Pourret, P., A, R., 2015. Projet ANR ASTER. Rapport de Tâche 4. Potentialité de stocks géologiques de terres rares en Europe et au Groenland. Rapport final. BRGM/RP-64910-FR, Orléans, France.
van de Kamp, P.C., 2016. Potassium distribution and metasomatism in pelites and schists: how and when, relation to post-depositional events. J. Sediment. Res. 86, 683–711.
Van Hoozen, C.J., Gysi, A.P., Harlov, D.E., 2020. The solubility of monazite (LaPO4, PrPO4, NdPO4, and EuPO4) endmembers in aqueous solutions from 100 to 250 °C. Geochim. Cosmochim. Acta 280, 302–316.
Vanderhaeghe, O., Laurent, O., Gardien, V., Moyen, J.-F., Gébelin, A., Chelle-Michou, C., Couzinié, S., Villaros, A., Bellanger, M., 2020. Flow of partially molten crust controlling construction, growth and collapse of the Variscan orogenic belt: the geologic record of the French Massif Central. Bull. Soc. Geol. Fr. 191, 25.
Vermeesch, P., 2018. IsoplotR: A free and open toolbox for geochronology. Geosci. Front. 9, 1479–1493.
Vidal, O., Dubacq, B., 2009. Thermodynamic modelling of clay dehydration, stability and compositional evolution with temperature, pressure and H2O activity. Geochim. Cosmochim. Acta 73, 6544–6564.
von Eynatten, H., Tolosana-Delgado, R., Karius, V., Bachmann, K., Caracciolo, L., 2016. Sediment generation in humid Mediterranean setting: Grain-size and source-rock control on sediment geochemistry and mineralogy (Sila Massif, Calabria). Sed. Geol. 336, 68–80.
Warr, L., Ferreiro Mählmann, R., 2015. Recommendations for Kübler index standardization. Clay Miner. 50, 283–286.
Wilby, P.R., Page, A.A., Zalasiewicz, J.A., Milodowski, A.E., Williams, M., Evans, J.A., 2007. Syntectonic monazite in low-grade mudrocks: a potential geochronometer for cleavage formation? J. Geol. Soc. 164, 53–56.
Wilkin, R.T., Barnes, H.L., 1997. Formation processes of framboidal pyrite. Geochim. Cosmochim. Acta 61, 323–339.
Wing, B.A., Ferry, J.M., Harrison, T.M., 2003. Prograde destruction and formation of monazite and allanite during contact and regional metamorphism of pelites: petrology and geochronology. Contrib. Miner. Petrol. 145, 228–250.
Wood, S.A., 1990. The aqueous geochemistry of the rare-earth elements and yttrium: 1. Review of available low-temperature data for inorganic complexes and the inorganic REE speciation of natural waters. Chem. Geol. 82, 159–186.
Yang, J., Torres, M., McManus, J., Algeo, T.J., Hakala, J.A., Verba, C., 2017. Controls on rare earth element distributions in ancient organic-rich sedimentary sequences: Role of post-depositional diagenesis of phosphorus phases. Chem. Geol. 466, 533–544.
Zhu, C., Rao, S., Hu, S., 2016. Application of illite crystallinity for paleo-temperature reconstruction: a case study in the Western Sichuan Basin, SW China. Carpathian J. Earth Environ. Sci. 11, 599–608.